

CARBON NANOTUBES

M.S. DRESSELHAUS

*Department of Electrical Engineering and Computer Science
and Department of Physics
Massachusetts Institute of Technology
Cambridge, Massachusetts 02139*

G. DRESSELHAUS

*Francis Bitter Magnet Laboratory
Massachusetts Institute of Technology
Cambridge, Massachusetts 02139*

AND

P.C. EKLUND, A.M. RAO

*Department of Physics and Astronomy
and Center for Applied Energy Research
University of Kentucky
Lexington, Kentucky 40506*

Abstract. A broad review of the structure and properties of carbon nanotubes is presented. Particular emphasis is given to the singularities in the one-dimensional density of states predicted for single-wall nanotubes of small diameter. The evidence provided by scanning tunneling microscopy and resonant Raman scattering experiments in support of these singularities in the one-dimensional density of states is presented. The remarkable electronic and mechanical properties of carbon nanotubes are also briefly reviewed and some potential applications for the nanotubes are suggested.

1. Carbon Nanotubes

The field of carbon nanotube research was launched in 1991 by the initial experimental observation of carbon nanotubes by transmission electron microscopy (TEM) [1], and the subsequent report of conditions for the synthesis of large quantities of nanotubes [2, 3]. Though early work was done on

coaxial carbon cylinders called multi-wall carbon nanotubes, the discovery of smaller diameter single-wall carbon nanotubes in 1993 [4, 5], which are cylinders of carbon atoms one atomic layer in thickness (see Figs. 1 and 2), greatly stimulated theoretical and experimental interest in the field. Other breakthroughs occurred with the discovery of methods to synthesize large quantities of single-wall nanotubes with a relatively small distribution of diameters [6, 7], thereby enabling experimental observation of the remarkable electronic, vibrational and mechanical properties of carbon nanotubes. Various experiments carried out thus far (e.g., high-resolution TEM, scanning tunneling microscopy (STM), conductance, and Raman scattering) are consistent with identifying single-wall carbon nanotubes as rolled up seamless cylinders of graphene sheets of sp^2 bonded carbon atoms organized into a honeycomb structure as a flat graphene sheet. Because of their very small diameters (down to ~ 0.7 nm) and relatively long lengths (up to \sim several μm), single-wall carbon nanotubes are prototype hollow cylindrical 1D quantum wires.

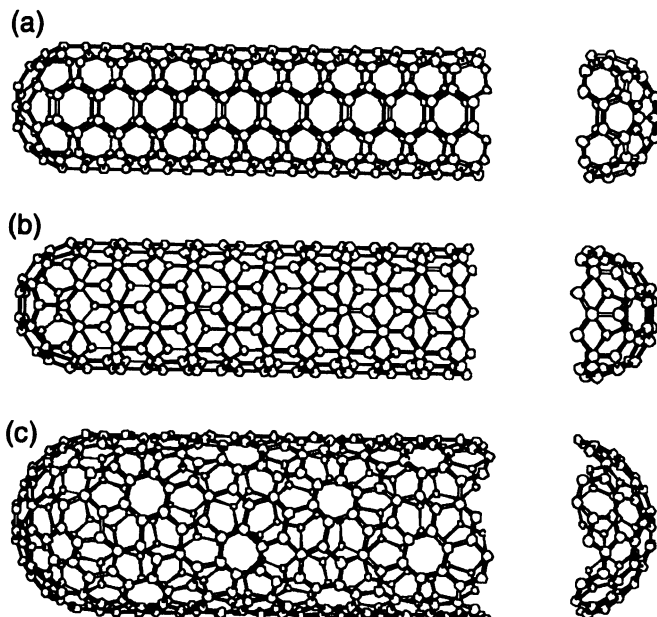


Figure 1. Schematic models for a single-wall carbon nanotubes with the nanotube axis normal to: (a) the $\theta = 30^\circ$ direction (an “armchair” (n, n) nanotube), (b) the $\theta = 0^\circ$ direction (a “zigzag” $(n, 0)$ nanotube), and (c) a general direction, such as \overrightarrow{OB} (see Fig. 2), with $0 < \theta < 30^\circ$ (a “chiral” (n, m) nanotube). The actual nanotubes shown here correspond to (n, m) values of: (a) $(5, 5)$, (b) $(9, 0)$, and (c) $(10, 5)$ as explained in Fig. 2 [8].

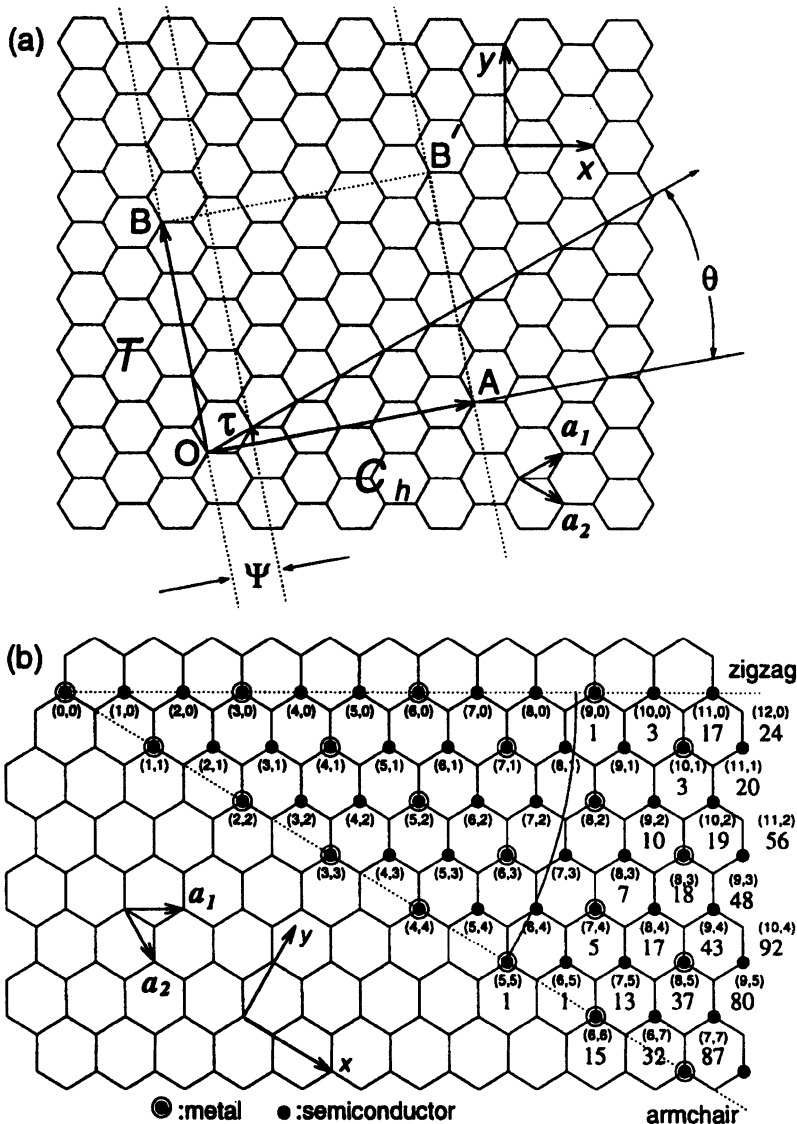


Figure 2. (a) The chiral vector \vec{OA} or $\vec{C}_h = n\hat{a}_1 + m\hat{a}_2$ is defined on the honeycomb lattice of carbon atoms by unit vectors \hat{a}_1 and \hat{a}_2 of a graphene layer and the chiral angle θ with respect to the zigzag axis ($\theta = 0^\circ$). Also shown are the lattice vector $\vec{OB} = \mathbf{T}$ of the 1D nanotube unit cell, the rotation angle ψ and the translation \vec{r} . The lattice vector of the 1D nanotube \mathbf{T} is determined by \vec{C}_h . Therefore the integers (n, m) uniquely specify the symmetry of the basis vectors of a nanotube. The basic symmetry operation for the carbon nanotube is $R = (\psi | \vec{r})$. The diagram is constructed for $(n, m) = (4, 2)$. (b) Possible chiral vectors \vec{C}_h specified by the pairs of integers (n, m) for general carbon nanotubes, including zigzag, armchair, and chiral nanotubes. According to theoretical calculations, the encircled dots denote metallic nanotubes, while the small dots are for semiconducting nanotubes [9].

1.1. SYNTHESIS

The earliest observations of carbon nanotubes with very small (nanometer) diameters [1, 10, 11] are shown in Fig. 3. Here we see results of high-resolution transmission electron microscopy (TEM) measurements, providing evidence for μm -long multi-layer carbon nanotubes, with cross sections showing several concentric coaxial nanotubes and a hollow core. One nanotube has only two coaxial carbon cylinders [Fig. 3(b)], and another has an inner diameter of only 2.3 nm [Fig. 3(c)] [1]. These carbon nanotubes were prepared by a carbon arc process (typical dc current of 50–100 A and voltage of 20–25 V), where carbon nanotubes form as bundles of nanotubes on the negative electrode, while the positive electrode is consumed in the arc discharge in a helium atmosphere [12]. Typical lengths of the arc-grown multi-wall nanotubes are $\sim 1 \mu\text{m}$, giving rise to an aspect ratio (length to diameter ratio) of 10^2 to 10^3 . Because of their small diameter, involving only a small number of carbon atoms, and because of their large aspect ratio,

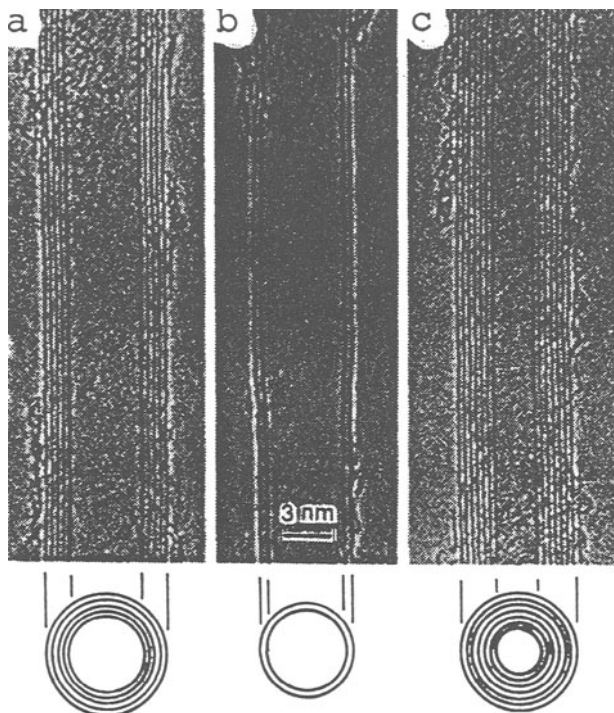


Figure 3. High-resolution TEM observations of three multi-wall carbon nanotubes with N concentric carbon nanotubes with various outer diameters d_o (a) $N = 5$, $d_o = 6.7 \text{ nm}$, (b) $N = 2$, $d_o = 5.5 \text{ nm}$, and (c) $N = 7$, $d_o = 6.5 \text{ nm}$. The inner diameter of (c) is $d_i = 2.3 \text{ nm}$. Each cylindrical shell is described by its own diameter and chiral angle [1].

carbon nanotubes are classified as one-dimensional (1D) carbon systems.

Most of the theoretical studies of carbon nanotubes have been on single-wall nanotubes and these studies have emphasized their 1D properties. In the multi-wall carbon nanotubes, the measured interlayer distance is 0.34 nm [1], comparable to the interlayer separation of 0.344 nm in turbostratic carbons.

Single-wall nanotubes were first discovered in an arc discharge chamber using a catalyst, such as Fe, Co and other transition metals, during the synthesis process [4, 5]. The catalyst is packed into the hollow core of the electrodes and isolated single-wall nanotubes condense in a cob-web-like deposit that sticks to the chamber walls. Single-wall nanotubes, just like the multi-wall nanotubes and also like conventional vapor grown carbon fibers [13], have hollow cores along the axis of the nanotube.

The diameter distribution of single-wall carbon nanotubes is of great interest for both theoretical and experimental reasons, since theoretical studies indicate that the physical properties of carbon nanotubes are strongly dependent on the nanotube diameter. Early results for the diameter distribution of Fe-catalyzed single-wall nanotubes (Fig. 4) show a diameter range between 0.7 nm and 1.6 nm, with the largest peak in the distribution occurring at 1.05 nm [4]. The smallest reported diameter for a single-wall carbon nanotube is 0.7 nm [4], the same as the diameter of the C₆₀ molecule (0.71 nm) [9]. Since the time of the earliest observation of single-wall carbon

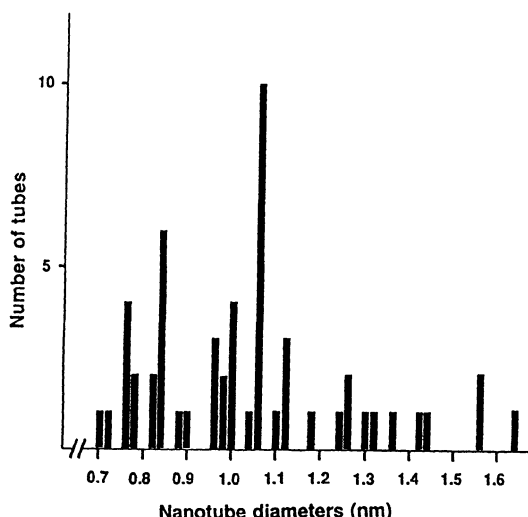


Figure 4. Histogram of the single-wall nanotube diameter distribution for Fe-catalyzed nanotubes [4]. A relatively small range of diameters are found, the smallest diameter corresponding to that for the fullerene C₆₀.

nanotubes, there have not been any reports of nanotubes with a smaller diameter than 0.7 nm.

The availability of single-wall carbon nanotubes for experimental studies was greatly increased by the discovery in 1996 of a more efficient synthesis route involving laser vaporization of graphite by Smalley's group [6]. Subsequent progress with the synthesis of single-wall carbon nanotubes [7] has provided a great stimulus to the field by making significant amounts of material available for experimental studies. Single-wall carbon nanotubes prepared by the Rice University group by the laser vaporization method utilize a Co-Ni/graphite composite target operating in a furnace at 1200°C. High yields with >70%-90% conversion of graphite to single-wall nanotubes have been reported [6, 14] when the Co-Ni catalyst/carbon ratio was 1.2 atom % Co-Ni alloy with equal amounts of Co and Ni added to the graphite (98.8 atom %). Flowing argon gas sweeps the entrained nanotubes from the high-temperature zone to a water-cooled Cu collector downstream, just outside the furnace [6].

Subsequently, other efficient synthesis routes were found for the preparation of "ropes" of single-wall carbon nanotubes. One very important approach uses a carbon arc method [7] to grow single-wall carbon nanotube arrays with a small distribution of nanotube diameters, very similar to the diameter distribution produced by the Rice group [6, 14]. Other groups worldwide are now also making single-wall carbon nanotube ropes using variants of the laser vaporization or carbon arc methods, as well as other methods such as synthesis from hydrocarbons in the vapor phase [15]. By using a variety of catalysts and growth conditions, it has been possible to grow single-wall nanotubes for which the peak in the nanotube diameter distribution can be varied from about 0.9 nm to 2.0 nm.

The nanotube material produced by the various synthesis methods appears in a scanning electron microscope (SEM) image as a mat of carbon ropes 10–20 nm in diameter and up to 100 μm or more in length (see Fig. 5), and these ropes are accompanied by varying amounts of amorphous carbon, catalyst, and other unwanted material, from which the nanotube ropes must be separated.

Under transmission electron microscope (TEM) examination, each nanotube rope is found to consist primarily of a bundle of single-wall carbon nanotubes aligned along a common axis (see Fig. 5). X-ray diffraction (which views many ropes at once) and transmission electron microscopy (which views a single rope) show that the diameters of the single-wall nanotubes have a strongly peaked narrow distribution of diameters. For the synthesis conditions used in the early work, the diameter distribution was strongly peaked at 1.38 ± 0.02 nm, very close to the diameter of an ideal (10,10) nanotube, as discussed below. X-ray diffraction measurements [6,

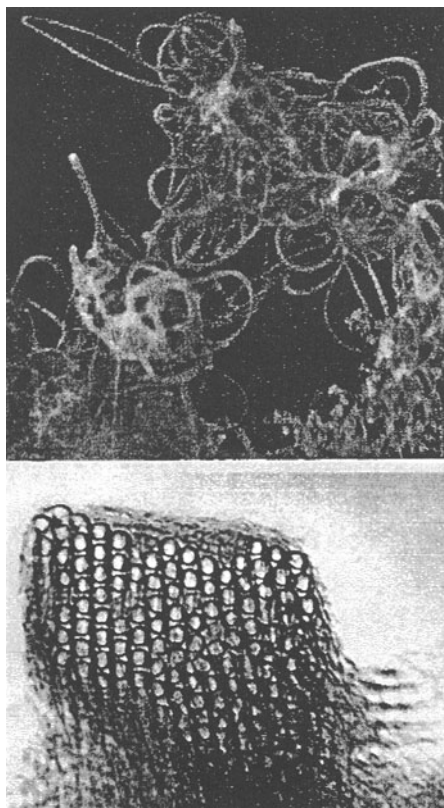


Figure 5. (a) Ropes of single-wall carbon nanotubes observed by scanning electron microscopy (SEM). The ropes are 10–20 nm thick and ~100 μm long. (b) At higher magnification, the TEM image shows that each rope contains a bundle of single-wall nanotubes with diameters of ~1.4 nm, arranged in a triangular lattice (with lattice constant 1.7 nm). The lower image is seen when the rope bends through the image plane of the transmission electron microscope (TEM) [6].

7] further showed that within these ropes, the single-wall nanotubes form a two-dimensional triangular lattice with a lattice constant of 1.7 nm, and an inter-tube separation of 0.315 nm at closest approach within a rope, in good agreement with prior theoretical modeling results [16, 17].

Whereas multi-wall carbon nanotubes require no catalyst for their growth, either by the laser vaporization or carbon arc methods, catalyst species are necessary for the growth of the single-wall nanotubes [6], while two different catalyst species seem to be needed to efficiently synthesize arrays of single wall carbon nanotubes by either the laser vaporization or arc methods. The detailed mechanisms responsible for the growth of carbon nanotubes are not yet well understood. The most probable diameter

and the width of the diameter distribution can be sensitively varied by the choice and composition of the catalyst species, the growth temperature and other growth conditions [18, 19].

1.2. STRUCTURE OF CARBON NANOTUBES

The structure of carbon nanotubes has been explored by high-resolution TEM and STM characterization studies, yielding direct confirmation that the nanotubes are cylinders derived from rolling up a single layer of the graphite honeycomb lattice (called a graphene sheet). Strong evidence that the nanotubes are cylinders and are not scrolls comes from the observation that the same numbers of walls appear on the left and right hand sides of thousands of TEM images of nanotubes, such as shown in Fig. 3. On the other hand, it is believed that under some growth conditions multi-wall nanotubes with scroll-like morphology can be synthesized. In pioneering work, Bacon in 1960 [20] synthesized graphite whiskers which he described as scrolls, using essentially the same conditions as for the synthesis of carbon nanotubes, except for Bacon's use of helium pressures, higher by an order of magnitude, to synthesize the carbon whisker scrolls.

Multi-wall carbon nanotubes also relate to vapor grown carbon fibers [13] of small diameter, which have cross sections with a morphology similar to the "rings of a tree" and at the center of these vapor grown carbon fibers is a multi-wall carbon nanotube, as shown in Fig. 6. In this figure we see that after a vapor grown carbon fiber is broken, a strong inner tube can be seen. It is believed that this inner carbon nanotube is first formed in the growth process, and that carbon feed-stock subsequently grows epitaxially in a thickening process [13]. Since vapor grown carbon fibers can be grown to diameters d_t less than 100 nm, there appears to be a continuum between the structure and properties of carbon fibers with diameters > 100 nm, carbon nanofibers with d_t in the range 10–100 nm, and finally the multi-wall nanotubes with $d_t < 10$ nm.

A single-wall carbon nanotube is conveniently characterized in terms of its diameter d_t , its chiral angle θ and its 1D (one-dimensional) unit cell, as shown in Fig. 2(a). Measurements of the nanotube diameter d_t and chiral angle θ are conveniently made by using STM (scanning tunneling microscopy) [21, 22] and TEM (transmission electron microscopy) techniques [4, 23], where θ has been normally defined by taking $\theta = 0^\circ$ and $\theta = 30^\circ$, to denote the zigzag and armchair nanotubes, respectively (see Fig. 1). While the ability to measure the diameter d_t and the chiral angle θ of individual single-wall nanotubes has been demonstrated, it remains a major challenge to determine d_t and θ for specific nanotubes that are used for an actual physical property measurements, such as scanning tunneling spectroscopy,

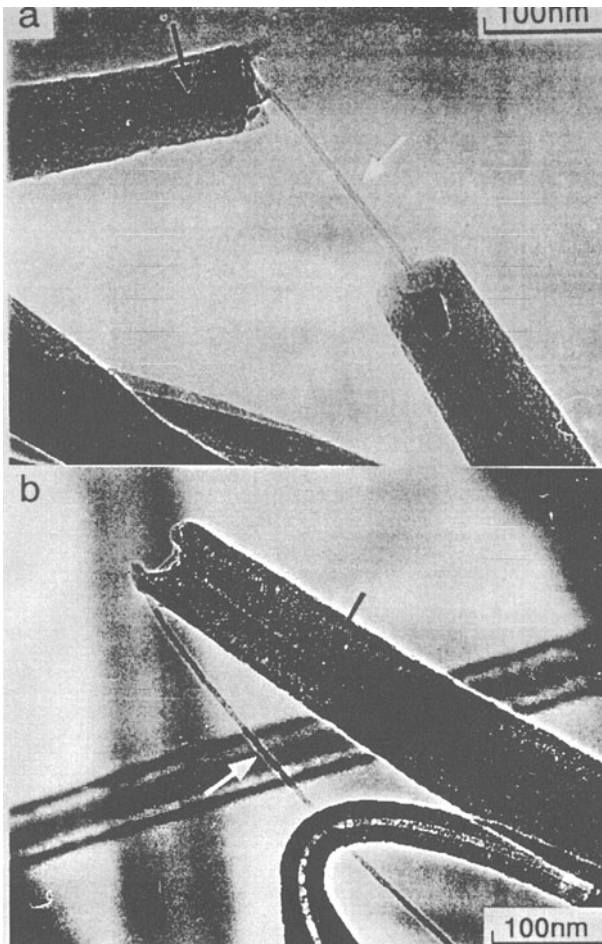


Figure 6. (a) Image of a broken vapor grown carbon fiber taken with a high-resolution field emission scanning electron microscope (SE-SEM). After the fiber is fractured, a strong inner core filament is pulled out, and is identified as a multi-wall carbon nanotube. (b) Image of a multi-wall nanotube emanating from the center of a vapor grown fiber. The arrow points to a nanotube coming from the central region of the fiber. These images indicate the connection between carbon nanotubes and vapor grown carbon fibers [13].

resistivity, Raman scattering, etc.

The circumference of any carbon nanotube is expressed in terms of the chiral vector $\vec{C}_h = n\hat{a}_1 + m\hat{a}_2$ which connects two crystallographically equivalent sites on a 2D graphene sheet [see Fig. 2(a)] [9]. The construction in Fig. 2(a) shows the chiral angle θ between the vector \vec{C}_h and the zigzag direction ($\theta = 0$), and shows the unit vectors \hat{a}_1 and \hat{a}_2 of the hexagonal

graphene honeycomb lattice. The chiral angle for armchair nanotubes is $\theta = 30^\circ$, and for chiral nanotubes $0 < \theta < 30^\circ$ (see Figs. 1 and 2). An ensemble of chiral vectors specified by pairs of integers (n, m) denoting the vector $\vec{C}_h = n\hat{a}_1 + m\hat{a}_2$ is given in Fig. 2(b) [24].

The cylinder connecting the two hemispherical caps of the carbon nanotube (see Fig. 1) is formed by superimposing the two ends of the vector \vec{C}_h and the cylinder joint is made along the two lines OB and AB' in Fig. 2(a). The lines OB and AB' are both perpendicular to the vector \vec{C}_h at each end of \vec{C}_h [9]. The intersection of OB with the first lattice point determines the fundamental 1D translation vector \vec{T} and thus defines the length of the unit cell of the 1D lattice for the nanotube [Fig. 2(a)]. The chiral nanotube, thus generated, has no distortion of bond angles other than distortions caused by the cylindrical curvature of the nanotube. Differences in the chiral angle θ and in the nanotube diameter d_t give rise to differences in the properties of the various graphene nanotubes. In the (n, m) notation for $\vec{C}_h = n\hat{a}_1 + m\hat{a}_2$, the vectors $(n, 0)$ or $(0, m)$ denote zigzag nanotubes and the vectors (n, n) denote armchair nanotubes. All other vectors (n, m) correspond to chiral nanotubes [24]. In terms of the integers (n, m) , the nanotube diameter d_t is given by

$$d_t = \sqrt{3}a_{C-C}(m^2 + mn + n^2)^{1/2}/\pi \quad (1)$$

where the nearest neighbor C–C distance for an nanotube is usually taken to be 1.44 Å, very close to the value of 1.42 Å for graphite. Correspondingly, the chiral angle θ is given by

$$\theta = \tan^{-1}(\sqrt{3}n/(2m + n)). \quad (2)$$

The number of hexagons, N , per 1D unit cell of a chiral nanotube is specified by the integers (n, m) and is given by

$$N = \frac{2(m^2 + n^2 + nm)}{d_R} \quad (3)$$

where d_R is the greatest common divisor of $(2n + m, 2m + n)$ and is given by

$$d_R = \begin{cases} d & \text{if } n - m \text{ is not a multiple of } 3d \\ 3d & \text{if } n - m \text{ is a multiple of } 3d, \end{cases} \quad (4)$$

where d is the greatest common divisor of (n, m) . The addition of a single hexagon to the honeycomb structure in Fig. 2(a) corresponds to the addition of two carbon atoms. As an example, application of Eq. (3) to the $(5, 5)$ and $(9, 0)$ nanotubes yields values of $N = 10$ and $N = 18$, respectively. Assuming a value $a_{C-C} = 1.44$ Å, we obtain values of $d_t = 6.88$ Å and $d_t = 7.15$ Å, respectively for $(5, 5)$ and $(9, 0)$ achiral nanotubes. However, for a $(6, 5)$ chiral nanotube with a diameter that is less than 10%

larger ($d_t = 7.57 \text{ \AA}$), the number of hexagons within the 1D unit cell is very large ($N = 182$). The 1D Brillouin zone for the nanotube is therefore much smaller than the one corresponding to a single 2-atom graphene unit cell. Because the local crystal structure of the nanotube is so close to that of a graphene sheet, and because the Brillouin zone is small, Brillouin zone-folding techniques have been commonly used to obtain approximate electron and phonon dispersion relations for carbon nanotubes with specific symmetry (n, m).

Because of the special atomic arrangement of the carbon atoms in a carbon nanotube, substitutional impurities are inhibited by the small size of the carbon atoms. Furthermore, the screw axis dislocation, the most common defect found in bulk graphite, is inhibited by the monolayer structure of the C₆₀ nanotube. For these reasons, we expect relatively few substitutional or structural impurities in single-wall carbon nanotubes. Multi-wall carbon nanotubes frequently show “bamboo-like” defects associated with the termination of inner shells, and pentagon-heptagon (5 – 7) pair defects are also found frequently in single-wall and multi-wall nanotubes [25].

1.3. ELECTRONIC STRUCTURE

Structurally, carbon nanotubes of small diameter are examples of a one-dimensional periodic structure along the nanotube axis. In single wall carbon nanotubes, confinement of the structure in the radial direction is provided by the monolayer thickness of the nanotube in the radial direction. Circumferentially, the periodic boundary condition applies to the enlarged unit cell that is formed in real space. The application of this periodic boundary condition to the graphene electronic states leads to the prediction of a remarkable electronic structure for carbon nanotubes of small diameter. We first present a brief summary of theoretical predictions, followed by a summary of experimental observations which lend support to these predictions. A more detailed discussion of this topic is found elsewhere in this volume [26].

The 1D electronic energy band structure for carbon nanotubes [27-31] is related to the energy band structure calculated for the 2D graphene honeycomb sheet used to form the nanotube. These calculations show that about 1/3 of the nanotubes are metallic and 2/3 are semiconducting, depending on the nanotube diameter d_t and chiral angle θ . It can be shown that metallic conduction in a (n, m) carbon nanotube is achieved when

$$2n + m = 3q, \quad (5)$$

where q is an integer. All armchair carbon nanotubes ($\theta = 30^\circ$) are metallic and satisfy Eq. (5) more generally. The metallic nanotubes, satisfying

Eq. (5), are indicated in Fig. 2(b) as encircled dots, and the small dots correspond to semiconducting nanotubes.

Calculated dispersion relations based on these simple zone folding considerations for tight binding energy bands are shown for metallic nanotubes $(n, m) = (5, 5)$ and $(9, 0)$ in Figs. 7(a) and (b), respectively, and for a semiconducting nanotube $(n, m) = (10, 0)$ in Fig. 7(c) [32]. These results are consistent with more detailed calculations of the band structure [26]. The calculated electronic structure can be either metallic or semiconducting depending on the choice of (n, m) as given by Eq. (5), although there is no difference in the local chemical bonding between the carbon atoms in the nanotubes, and no doping impurities are present [24].

These surprising results can be understood on the basis of the electronic structure of a graphene sheet which is found to be a zero gap semiconductor [34] with bonding and antibonding π bands that are degenerate at the K -point (zone corner) of the hexagonal 2D Brillouin zone. The periodic boundary conditions for the 1D carbon nanotubes of small diameter permit only a few wave vectors to exist in the circumferential direction, and these wave vectors k satisfy the relation $n\lambda = \pi d_t$ where $\lambda = 2\pi/k$ is the de Broglie wavelength. Metallic conduction occurs when one of these allowed wave vectors k passes through the K -point of the 2D Brillouin zone, where the valence and conduction bands are degenerate because of the special symmetry of the 2D graphene lattice [35].

As the nanotube diameter increases, more wave vectors become allowed for the circumferential direction, so that the nanotubes become more two-dimensional and the semiconducting band gap disappears, as is illustrated

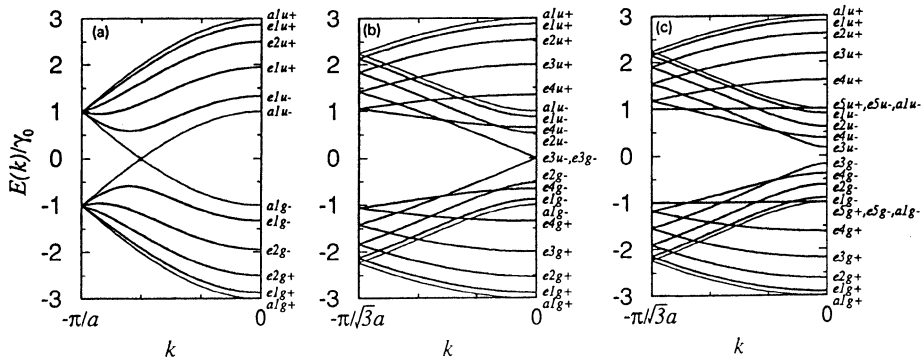


Figure 7. One-dimensional energy dispersion relations for (a) armchair $(5, 5)$ nanotubes, (b) zigzag $(9, 0)$ nanotubes, and (c) zigzag $(10, 0)$ nanotubes. The energy bands with a symmetry are non-degenerate, while the e -bands are doubly degenerate at a general wave vector k [24, 32, 33].

in Fig. 8, which shows the semiconducting band gap to be proportional to the reciprocal nanotube diameter $1/d_t$. At a nanotube diameter of $d_t \sim 3\text{ nm}$ (Fig. 8), the band gap becomes comparable to thermal energies at room temperature, showing that small diameter nanotubes are needed to observe 1D quantum effects.

Calculations of the electronic structure for two concentric nanotubes show that pairs of concentric metal-semiconductor or semiconductor-metal nanotubes are stable [37]. From these results, one could imagine designing an electronic shielded wire device less than 3 nm in diameter, consisting of two concentric graphene nanotubes with a smaller diameter metallic inner nanotube surrounded by a larger diameter semiconducting (or insulating) outer nanotube. Such concepts could in principle be extended to the design of tubular metal-semiconductor all-carbon devices without introducing any doping impurities [24]. The observation of coaxial metallic and semicon-

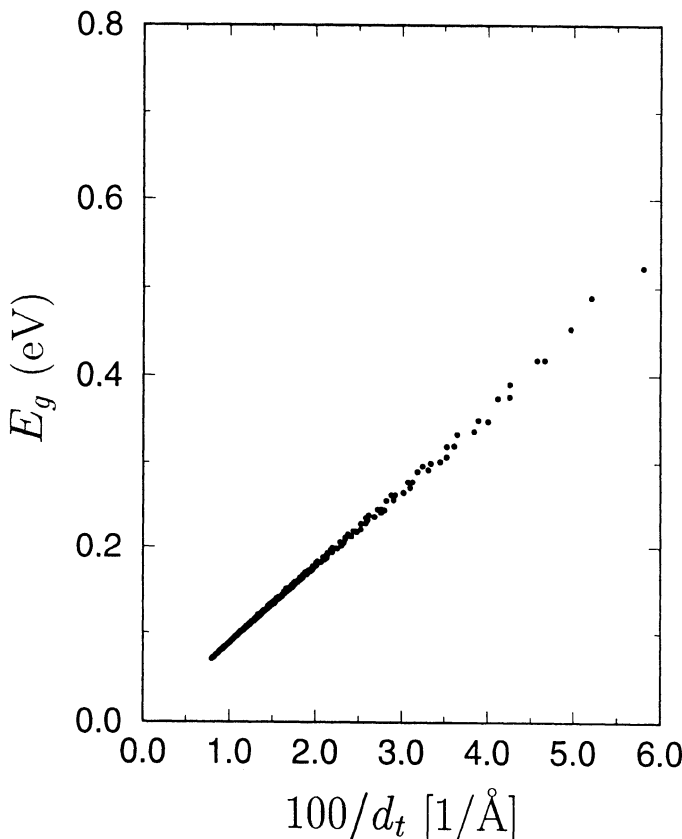


Figure 8. The energy gap E_g for a general chiral single-wall carbon nanotube as a function of $100\text{ \AA}/d_t$, where d_t is the nanotube diameter in \AA [36].

ducting nanotube structures, such as the one reported for several coaxial BN tubes grown on either side of a few coaxial carbon nanotubes [38], are very stimulating developments for possible future device applications of nanotubes.

Closely related to the 1D dispersion relations for the carbon nanotubes in Fig. 7 is the 1D density of states shown in Fig. 9 for: (a) a semiconducting (10,0) zigzag carbon nanotube, and (b) a metallic (9,0) zigzag carbon nanotube. The results show sharp singularities associated with the $(E - E_0)^{-1/2}$ dependence expected for the 1D density of states about each subband edge at E_0 which can be seen in Fig. 7 at $k = 0$. The results in Fig. 9 further show that the metallic nanotubes have a small, but non-vanishing 1D density of states at the Fermi level (which is at $E = 0$ in Fig. 9), and this non-vanishing density of states is independent of energy until the energies of the first subband edges of the valence and conduction bands are reached. In contrast, for a 2D graphene sheet (dashed curve), the 2D density of states is zero at the Fermi level (where also $E = 0$ in Fig. 9), and varies linearly with energy, as we move away from the Fermi level. Furthermore, the density of states for the semiconducting 1D nanotubes is zero throughout the band gap, as shown in Fig. 9(a), and their band-gap energy E_g is equal to the energy difference between the two singularities in the 1D density of states that span the Fermi level. Because of these singularities in the density of states, high optical absorption is expected when the photon energy matches the energy separation between an occupied electron state and one that is empty. This situation occurs at the band gap for the semiconducting nanotubes, but also at higher energies for transitions from an occupied subband edge state to the corresponding unoccupied edge state. Such transitions between subband edge states can occur for both semiconducting and metallic nanotubes. Comparing the density of states curves in Fig. 9, we see that the smallest energy separation between subband edge states for the semiconducting nanotube (10,0) is much smaller than the corresponding separation between subband edges for the metallic (9,0) nanotube. These general characteristics predicted for the 1D electronic density of states have recently been confirmed by low temperature STM/STS studies carried out on single-wall carbon nanotubes [21, 22, 39].

Experimental measurements to test the remarkable theoretical predictions of the electronic structure of carbon nanotubes are difficult to carry out because of the strong dependence of the predicted electronic properties on nanotube diameter and chirality. Difficulties arise from the great experimental challenges in making electronic or optical measurements on individual single-wall nanotubes because of their tiny size, and further challenges arise in making such demanding measurements on individual nanotubes that have been characterized with regard to diameter and chiral angle (d_t

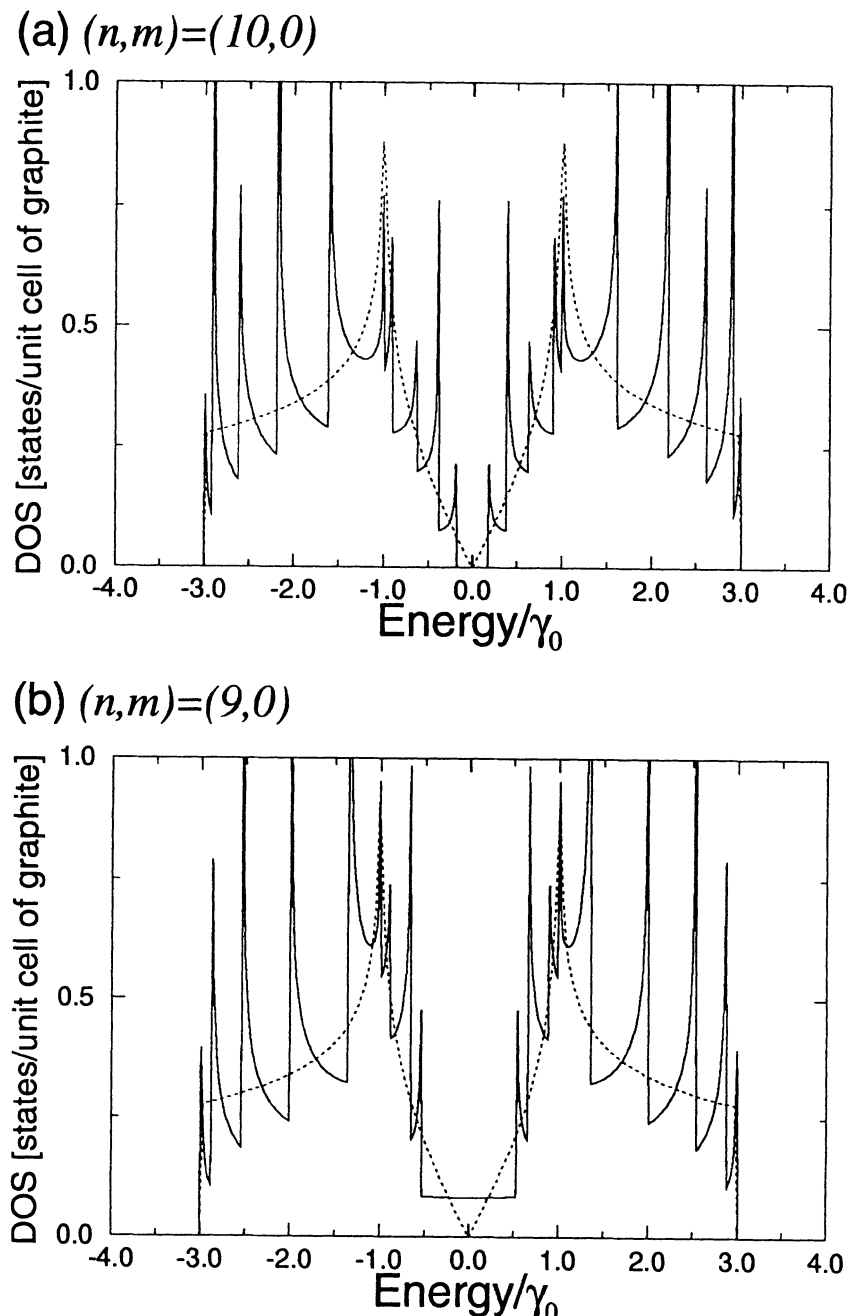


Figure 9. Electronic 1D density of states per unit cell of a 2D graphene sheet for two $(n, 0)$ zigzag nanotubes: (a) the $(10, 0)$ nanotube which has semiconducting behavior, (b) the $(9, 0)$ nanotube which has metallic behavior. Also shown in the figure is the density of states for the 2D graphene sheet (dotted line) [37].

and θ). Despite these difficulties, pioneering work has already been reported on experimental observations relevant to the electronic structure of individual multi-wall nanotubes, on bundles of multi-wall nanotubes, on a single bundle or rope of single-wall carbon nanotubes, and even on an individual single-wall nanotube.

The most promising present technique for carrying out sensitive measurements of the electronic properties of individual nanotubes is scanning tunneling spectroscopy (STS) because of the ability of the tunneling tip to sensitively probe the electronic density of states of either a single-wall nanotube [21, 22, 40] or the outermost cylinder of a multi-wall nanotube [41], due to the exponential dependence of the tunneling current on the distance between the nanotube and the tunneling tip. With this technique, it should be possible to carry out both STS and scanning tunneling microscopy (STM) measurements on the same nanotube and therefore to measure the nanotube diameter d_t concurrently with the STS spectrum [41], and chiral angle θ as well [22].

In early STM/STS studies, more than nine individual multi-wall nanotubes with diameters d_t ranging from 1.7 to 9.5 nm were examined. Topographic STM measurements were made on the same nanotubes to obtain the maximum height of the nanotube relative to the gold substrate, thus determining the diameter of each individual nanotube [41]. Then switching to the STS mode of operation, current–voltage (I vs. V) plots were made on the same region of the same nanotube as was characterized for its diameter by the STM measurement. Their results provided evidence for both metallic and semiconducting outer walls for their multi-wall nanotubes [41]. The results for all their semiconducting nanotubes showed a linear dependence of their energy gaps on $1/d_t$, consistent with the predicted functional form shown in Fig. 8.

Subsequently more detailed STM/STS experiments were carried out at low temperature on individual single-wall carbon nanotubes [21, 22]. The images in the STM mode were at atomic resolution, allowing characterization of individual single-wall nanotubes in the scanning tunneling mode (STM) according to their diameter and chiral angle [or equivalently their (n, m) indices found by solving Eqs. (1) and (2)] [21, 23]. Measurements of dI/dV in the STS mode, shown in Fig. 10, yielded the 1D density of states (which is proportional to dI/dV) for both metallic and semiconducting nanotubes.

The combined STM/STS studies [21, 23] are consistent with: (1) about 2/3 of the nanotubes being semiconducting, and 1/3 being metallic; (2) the density of states exhibiting singularities characteristic of expectations for 1D systems; (3) E_g for the semiconducting nanotubes is proportional to $1/d_t$ with $E_g = 2\gamma_0 a_{C-C}/d_t$; and (4) the nearest neighbor overlap integral

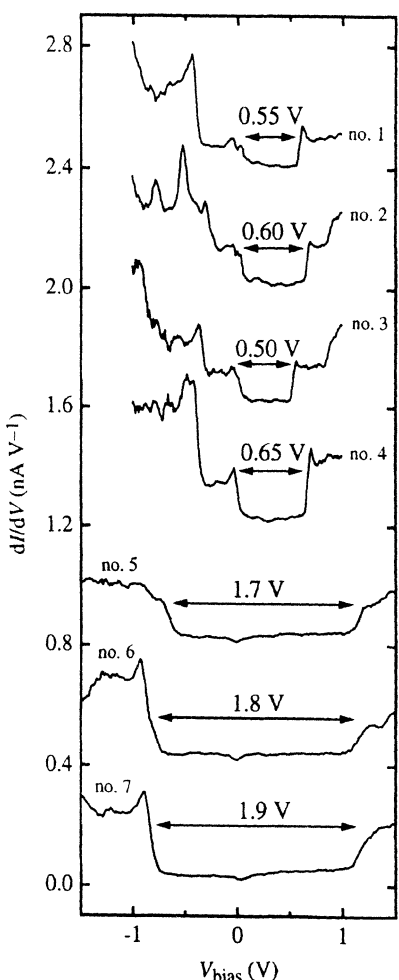


Figure 10. Derivative of the current-voltage (dI/dV) curves obtained by scanning tunneling spectroscopy on various nanotubes. Nanotubes #1–6 are chiral and #7 is zigzag. The bias voltage V_{bias} applied to the sample corresponds to the energy relative to the nanotube Fermi level. The diameter and chiral angle of the nanotubes are respectively: #1 with 1.4 nm, $\theta = 5^\circ$; #2 with 1.4 nm, $\theta = 26^\circ$; #3 with 2.0 nm, $\theta = 23^\circ$; #4 with 1.2 nm, $\theta = 6^\circ$; #5 with 1.7 nm, $\theta = 21^\circ$; #6 with 1.4 nm, $\theta = 4^\circ$; and #7 with 1.1 nm, $\theta = 0^\circ$, $(n, 0) = (14, 0)$. Energy differences between the lowest conduction band and highest valence band spike-like features are indicated by the arrows. Nanotubes #1–4 typically have values of ~ 0.5 – 0.6 V between these 1D density of states peaks (see Fig. 7), and are identified as being semiconducting, whereas nanotubes #5–7 have larger values of ~ 1.7 – 1.9 V, indicating that these are metallic. The small dips seen at zero bias, in some of the curves, are due to an experimental artifact [21].

(or transfer integral) γ_0 is found to be 2.7 eV from the STS data [21], in good agreement with theoretical predictions. In addition, these measurements showed that the density of electronic states near the Fermi level is zero for semiconducting nanotubes, and non-zero for metallic nanotubes [21]. These density of states curves are also important for explaining the quantum effects observed in the resonant Raman experiments on carbon nanotubes discussed in §1.6. More detailed future STM/STS studies should provide a quantitative determination of the band parameters governing the 1D electronic structure for carbon nanotubes.

1.4. TRANSPORT PROPERTIES

The measured transport properties of carbon nanotubes depend on whether the transport measurements are carried out on individual single-wall nanotubes, on a single rope or bundle containing many single-wall nanotubes (see Fig. 5), on an individual multi-wall nanotube or on other nanotube samples. These differences arise in part from different scattering mechanisms and different contact problems that come into play for each type of sample. For example, a bundle or rope of single-wall nanotubes contains conduction paths between nanotubes that are not present for isolated single-wall nanotubes. Also, it is difficult to make good electrical contacts to each nanotube in the rope. For the case of a mat of material containing single nanotube ropes, there are contributions to the conduction from non-single-wall nanotube material. In addition, the relatively poor electrical contact between adjacent single-wall nanotubes within a single rope and between single wall nanotubes in different ropes that must be taken into account. Because of their large length to diameter ratio, electrical contacts have been made to these nanometer size structures using modern lithographic techniques [42], but such processes can introduce strains and local fields that could significantly affect the measurements.

The first transport measurement on an individual isolated single-wall carbon nanotube was made on a nanotube 1.3 nm in diameter resting on a

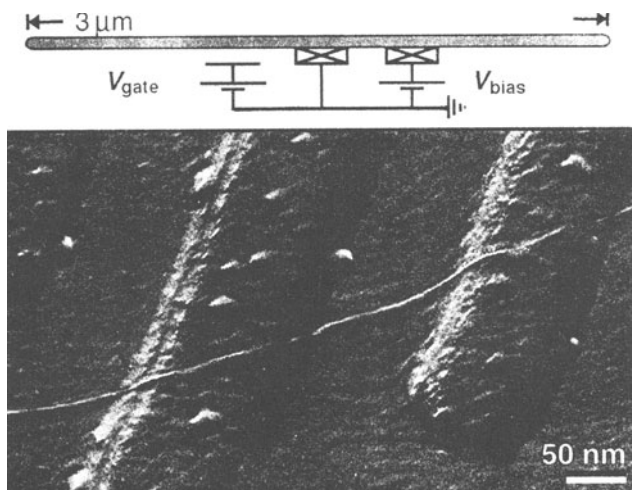


Figure 11. AFM tapping-mode image of a thin (~ 1 nm) carbon nanotube on top of a Si/SiO₂ substrate with two 15 nm-thick and 140 nm wide Pt electrodes. A schematic circuit diagram for the transport experiments shown in Fig. 12 is given at the top [43].

Si/SiO₂ substrate, with two Pt electrodes (15 nm-thick and 140 nm wide) used to measure the current vs. bias voltage V_{bias} , where V_{bias} denotes the difference in the chemical potential between the two electrodes, μ_1 and μ_2 , as shown in Fig. 11 [43]. A gate voltage V_{gate} , was used to change the electrostatic potential seen by the nanotube (see Fig. 11), so that the gate voltage V_{gate} changes the position of the energy levels of the nanotube relative to the chemical potentials, μ_1 and μ_2 . Because of the finite length ($L = 3 \mu\text{m}$) of the nanotube, the one-dimensional energy band is split into quantized energy levels whose spacing is $\Delta E = h\nu_F/2L$, and the nanowire behaves like a single large molecule that is weakly coupled to the external electrodes. Figure 12(b) shows that tunneling occurs when one of these quantum dot levels falls in the range of the tunneling window between μ_1 and μ_2 , as shown on the bottom right of Fig. 12. The experiments shown in Fig. 12 yield a value of $\Delta E \sim 0.6 \text{ meV}$, where the Fermi velocity is taken as $v_F \sim 8.1 \times 10^5 \text{ m/s}$ [43]. Single-wall carbon nanotubes thus provide a unique system for studying the electronic structure of large single molecules and for observing single molecule transistor effects [44-46].

The observation of coherent electron transport is an important result since interactions with the environment (such as the van der Waals interaction with the substrate), structural imperfections, bends or twists in the tube can cause the conduction electrons to become localized. Based on tight-binding model to study the effects of disorder on the transport properties of armchair tubes [47], it was found that for a fixed amount of disorder, the mean free path of the conduction electrons increases with decreasing nanotube diameter leading to long localization lengths ($\sim 10 \mu\text{m}$) and ballistic transport for small diameter nanotubes ($d_t \sim 1.4 \text{ nm}$).

The I vs. V_{bias} curves, obtained at gate voltages of 88.2 mV (curve A), 104.1 mV (curve B) and 120.0 mV (curve C) at 5 mK, are shown in Fig. 12(a) [43]. In these measurements the nanotube makes weak electrical contact with the electrodes, as indicated by the high (megohm) contact resistances. Curves A, B, C all show plateaus of non-zero current, which present clear evidence for ballistic transport in which a conducting channel is in the tunneling window range of $V_{\text{bias}} = (\mu_1 - \mu_2)/e$ (see lower right of the figure). The position of the steps in the I vs. V_{bias} curves is changed by increasing the gate voltage. Coulomb charging effects of the nanotube were also observed at low temperature, whereby the nanotube, considered as a capacitor with a capacitance C , has a thermal energy $k_B T$ smaller than the charging energy E_c for a single electron, where $k_B T < E_c = e^2/2C$. A Coulomb blockade is observed when the current flow is blocked by the energy E_c which shifts levels out of the bias window between μ_1 and μ_2 . Thus, current flow in Fig. 12(b) appears only when $V_{\text{bias}} > E_c$. Systematic studies of the Coulomb blockade phenomena as a function of nanotube

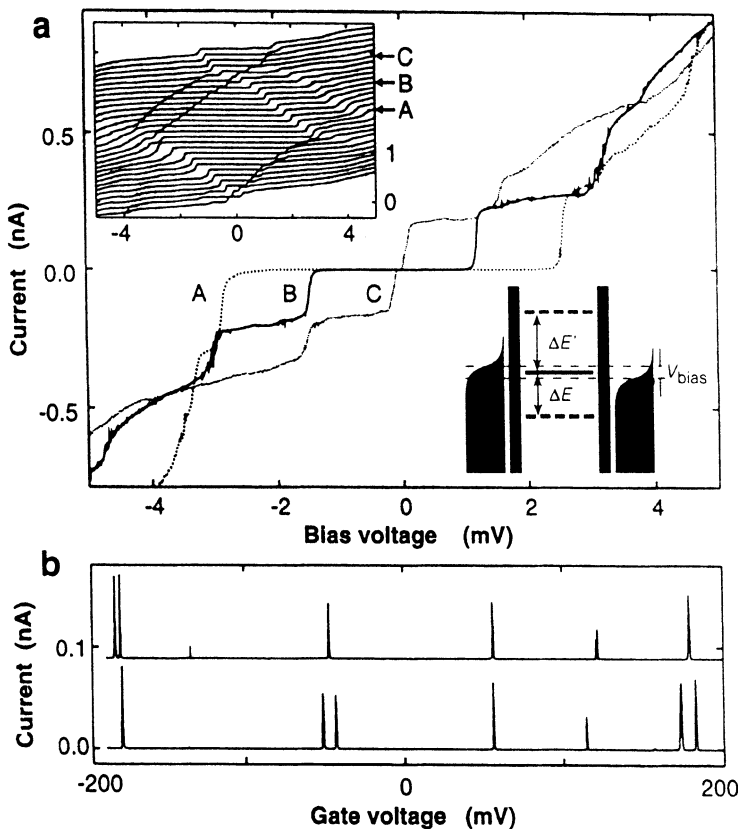


Figure 12. (a) Current-voltage curves of a carbon nanotube at a gate voltage of 88.2 mV (curve A), 104.1 mV (curve B) and 120.0 mV (curve C). In the upper left inset, a number of I vs V_{bias} curves are shown with V_{gate} ranging from 50 mV (bottom curve) to 136 mV (top curve). In the lower right, the window for tunneling is shown when a quantum-dot level lies within this window. (b) The two traces of current versus gate voltage at $V_{bias} = 30 \mu V$ were performed under the same conditions and represent a bistability of the system [43].

diameter in armchair nanotubes and in other metallic nanotubes are of great current interest [45]. Since the nanotube energy levels can be modified by V_{gate} , the step positions shown in the inset of Fig. 12(a) can be changed smoothly as a function of V_{gate} . The phenomena observed in Fig. 12 can be understood by steps in the quantum conductance, and charging effects associated with the micro-capacitances of the nanotube and the gate.

Direct observation of steps in the conductance, which is the characteristic behavior expected for 1D conductors has been reported, using a clever technique to make good ohmic contacts to the outer wall of a multiwall carbon nanotube [48]. The magnitude of the observed conductance step is

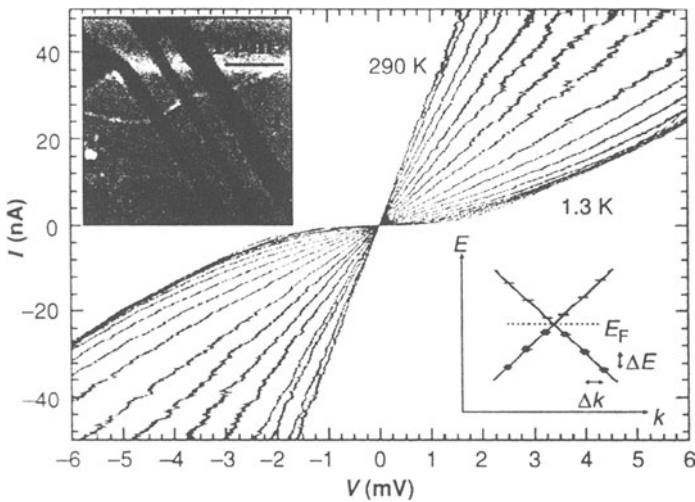


Figure 13. I vs. V characteristics of a single 12-nm-diameter rope made up about 60 single-wall nanotubes with diameters of about 1.4 nm. The I vs. V curves are taken between contacts #2 and #3 (left inset) and at various temperatures between 1.3 K and 290 K. The right inset schematically shows energy levels near the Fermi energy. These energy levels are quantized (quantum dot levels) because of the finite length of nanotube [52].

$G_0 = 2e^2/h = (12.9 \times 10^3 \Omega)^{-1}$, indicative of a single conductance channel, whereas prior theoretical predictions [49-51] suggested that carbon nanotubes should have two conductance channels.

Transport measurements (current-voltage) on a single 12 nm-diameter rope, containing about 60 single-wall nanotubes of 1.4 nm-diameter [52], are shown in Fig. 13 for the rope segment between contacts 2 and 3 (left inset). At room temperature, the I vs. V characteristics gives ohmic behavior, while the reduction in conductance near $V = 0$ for $T < 10$ K is interpreted in terms of a small band gap associated with single electron tunneling within the framework of the Coulomb blockade effect. These data further show an increase in resistance with decreasing temperature over a wide temperature range from 1.3 K to 290 K. Deviations from Fermi-liquid behavior in single wall nanotubes were predicted owing to their strongly one-dimensional properties [43] and to tube-tube interactions [53], and subsequently observed from conductance measurements on single wall nanotubes bundles as a function of temperature and gate voltage [54], showing that the Coulomb interactions between the electrons near the Fermi level lead to a Luttinger-liquid behavior in carbon nanotubes. In another experiment on a single rope, about a 10% increase of the resistivity was reported from 50 K to 280 K [55], while a decrease in the resistivity with

increasing T was found below 50 K. The reasons for these discrepancies in the temperature-dependent resistivity of carbon nanotubes within a single rope are not presently understood, though it is believed that sample-to-sample variations could be significant. It is also believed that inter-tube transport phenomena between single-wall nanotubes in a rope make an essential contribution to the observed transport properties.

The resistance measurements for various kinds of nanotube samples by a number of different groups generally show that there are metallic and semiconducting nanotubes, as was first predicted theoretically [56-58]. Theoretical studies [49, 59-62] using a tight binding model have further shown that a pentagon-heptagon pair defect introduced into the hexagonal network of a single carbon nanotube could change the electronic structure of a previously metallic or semiconducting tube to form a metal-semiconductor junction within a single nanotube. A near-ideal rectification behavior was observed [63] in one of the current-voltage responses obtained for a single carbon nanotube rope using a scanning tunneling microscope. The most common response which provides evidence for the existence of an on-tube or on-rope "nano-device" was a transition from the nearly symmetric nonlinear conductance to a highly nonlinear asymmetric conductance state involving current jumps by two to four orders of magnitude [63].

Resistivity values in the range $10^{-4} - 10^{-3} \Omega\text{cm}$ have been reported for metallic nanotubes, while the room temperature resistivity of semiconducting nanotubes is much higher, $\sim 10^1 \Omega\text{cm}$. Semiconducting nanotubes exhibit a slope in a plot of $\log R$ versus $1/T$, which indicates an energy gap in the range 0.1–0.3 eV, which is roughly consistent with theoretical values of the energy gap for the corresponding nanotube diameters. On the other hand, for the metallic nanotubes, large fluctuations from sample to sample were reported for the absolute values of the resistance and in the temperature dependence of the resistance over a wide temperature range from 4 K to 300 K. Differences in behavior from sample to sample and from group to group may be associated with the different (n, m) distribution of nanotubes in the samples under investigation, to structural defects, differences in the diameters and chiralities of the constituent nanotubes, difference in the methods used to make contacts, electrical fields associated with the contacts, and differences in the temperature range for the experiments.

In the low-temperature regime, weak localization and universal conductance phenomena have been reported for an individual multi-wall nanotube with an outer diameter of 20 nm [58]. Research opportunities remain for systematic studies of weak localization and universal conductance phenomena in the small diameter range where 1D phenomena are expected. There is particular interest in studying the dependence of these phenomena on nanotube diameter and chirality. Theoretical models are needed to explain the

weak localization and universal conductance phenomena observed thus far in carbon nanotubes and to predict the effect of nanotube diameter and chirality on these phenomena.

The first measurements of the Seebeck coefficient S were made on tangled mats of bundles of single-wall nanotubes, and yielded surprisingly large room temperature values $S(300\text{K}) \sim +50 \pm 10 \mu\text{V/K}$, and a strongly non-linear $S(T)$ temperature dependence [64, 65], in sharp contrast to the small value of $S(300\text{K}) \sim +3 \pm 1 \mu\text{V/K}$ and the essentially linear $S(T)$ dependence found in graphite. Moreover, the $R(T)$ curves in single wall nanotubes exhibited a shallow minimum at $T^* \sim 150 - 300\text{ K}$, and a crossover from a metallic temperature dependence ($dR/dT > 0$, at $T > T^*$) to a non-metallic dependence ($dR/dT \ll 0$, at $T \ll T^*$) [66-68]. At present, there is no consensus on possible physical mechanisms to explain the large values and the non-linear T -dependence of $S(T)$, as well as the upturn of R below T^* . Tentative explanations include weak localization [64, 66, 67], heterogeneity of the sample [68], tube-tube interactions [69], contributions from the semiconducting nanotubes present in the nanotube bundles [64], and a Kondo mechanism [70].

Further experimental study has shown that $R(T)$ and $S(T)$ of mat samples [see Fig. 5(a)] are dramatically affected by the presence and identity of the residual transition metal catalyst M (where M = Ni, Co, Fe) [70]. This anomalous transport was attributed, in part, to the interaction between the localized $3d$ -electrons of the catalyst atoms in contact with the tube walls and the conduction electrons in the nanotubes through a Kondo mechanism. A post-synthesis iodine treatment was shown to form Kondo-inactive metal-iodide complexes to suppress the Kondo interaction, and produce "M-independent" electrical transport properties that approach the anticipated intrinsic metallic single wall nanotube behavior [66, 71].

Regarding the thermal conductivity κ in undoped nanotube mats, κ was found to be large (comparable to that of diamond or in-plane graphite) and dominated by phonons within the $8 < T < 350\text{ K}$ range. Upon cooling, κ decreased monotonically and showed a linear T dependence below 30 K [72], as might be expected for a 1D phonon system.

Doping the mat sample with Cs was found to decrease $S(300\text{K})$ to $\sim -7 \mu\text{V/K}$ [71], as expected for an ordinary metal. The electrical transport properties of single wall nanotubes are significantly modified by doping. In particular, upon doping with either alkali metals (K, Cs) [66, 71] or halogens (Br, I) [65, 66], the dc resistivity values of nanotube mats decrease dramatically, and the $R(T)$ dependence usually becomes more metallic [65-68]. Only the I-doped nanotube samples were found to be air-stable [66].

The *in-situ* four-probe dc resistance (R) measurements of Cs- and K-doped single-wall carbon nanotube mats [71] have shown that, with increas-

ing dopant exposure, the mat resistance passes through a minimum R for optimal Cs-doping, while for K-doping, the mat resistance decreases monotonically and saturates, suggesting that the diameter of the alkali metal ion plays a role in the transport properties of the tube bundles. A doping-induced decrease in R by factors of ~ 120 and ~ 40 were observed for Cs- and K-doped nanotube mats, respectively [71].

1.5. PHONON MODES

The phonon dispersion relations in a carbon nanotube can be obtained from those of the 2D graphene sheet by using the same zone folding approach [73-75] as was used to find the 1D electronic dispersion relations [35, 76]. Because of the very weak interplanar interactions, the phonon dispersion relations for graphite in the basal plane (see Fig. 14) provide a good first approximation for the 2D phonon dispersion relations of an isolated graphite plane, which is called a graphene sheet. The 1D dispersion relations assume that the lengths of the nanotubes are much larger than their diameters, so that the nanotubes can be described in the 1D limit where the nanotubes have infinite length, the k points are continuous, and the contributions from the carbon atoms in the caps can be neglected. Just as for the case of the electronic structure, the phonon dispersion relations depend on the nanotube diameter and chirality. We give explicit results here for the vibrational mode classifications for the symmetry types. Then we discuss the symmetries of the 4 modes for which the frequency vanishes ($\omega \rightarrow 0$) in the limit as the wave vector approaches the zone center ($k \rightarrow 0$), as well as the symmetries of optically-active Raman and infrared modes, with special attention given to the fact that the number of modes that are optically active depend only on the symmetry type and not on the nanotube diameter or chiral angle.

For a nanotube with N hexagons per 1D unit cell [see Fig. 2(a)], there are two carbon atoms per hexagon and 3 vibrational degrees of freedom per C atom to give a total of $6N$ degrees of freedom per 1D unit cell. For armchair and zigzag nanotubes $N = 2n$, but for chiral nanotubes, Eq. (3) is used to find N . The $6N$ degrees of freedom correspond to the following symmetry types for the various nanotube symmetries. The symmetries of the vibrational modes are found by taking a direct product of the irreducible representations of the vector with the irreducible representations contained in the equivalence transformation for the carbon atoms within the 1D unit cell. The character of the equivalence transformation for an operation R of the point group is defined by the number of atoms within the unit cell which do not change their position when the symmetry operation is carried out. For (n, n) armchair nanotubes for which $n/2$ is even, the vibrational modes

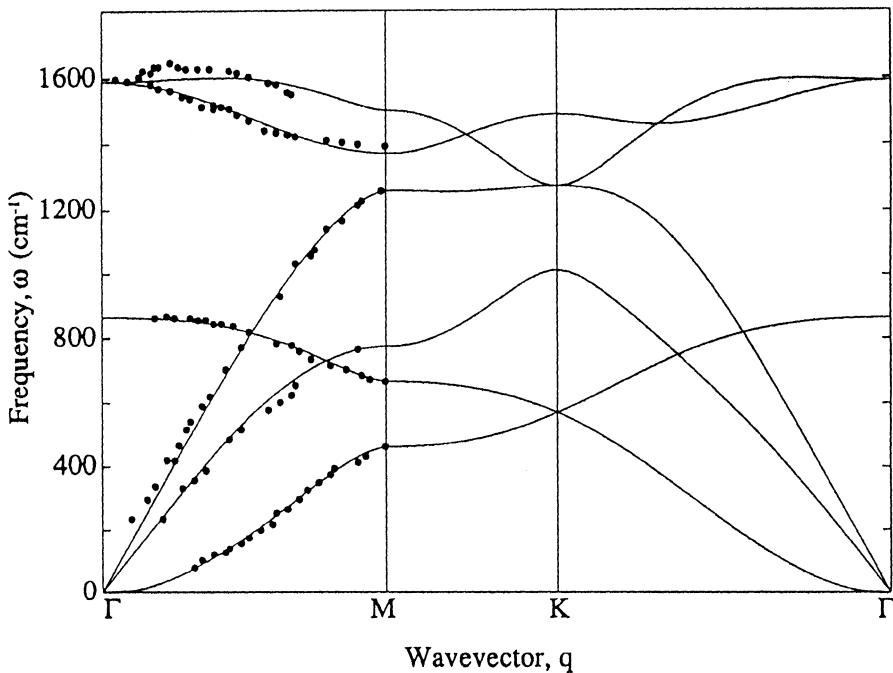


Figure 14. The phonon dispersion relations for graphite plotted along high-symmetry in-plane directions. Experimental points from neutron scattering and electron energy loss spectra were used to obtain values for the force constants and to determine the phonon dispersion relations throughout the Brillouin zone [73].

are decomposed according to the following irreducible representations of the point group D_{nh} :

$$\begin{aligned} \Gamma_{(n,n)}^{\text{vib}} = & 4A_{1g} + 2A_{1u} + 4A_{2g} + 2A_{2u} + 2B_{1g} \\ & + 4B_{1u} + 2B_{2g} + 4B_{2u} + 4E_{1g} + 8E_{1u} + 8E_{2g} \\ & + 4E_{2u} + \cdots + 4E_{(n/2-1)g} + 8E_{(n/2-1)u} \quad (n/2 = \text{even integer}). \end{aligned} \quad (6)$$

If $n/2$ is odd [such as for $(n, m) = (10, 10)$], the 4 and 8 are interchanged in the last two terms in Eq. (7).

Armchair nanotubes (n, n) , for which n is an odd number of unit cells in the circumferential direction, have D_{nd} symmetry and have vibrational

modes with the following symmetries:

$$\begin{aligned}\Gamma_{(n,n)}^{\text{vib}} = & \quad 3A_{1g} + 3A_{1u} + 3A_{2g} + 3A_{2u} \\ & + 6E_{1g} + 6E_{1u} + 6E_{2g} + 6E_{2u} \\ & + \cdots + 6E_{[(n-1)/2]g} + 6E_{[(n-1)/2]u} \quad (n = \text{odd integer}).\end{aligned}\quad (7)$$

For zigzag $(n, 0)$ nanotubes with odd n , the vibrational modes are described by the D_{nd} point group and have symmetries:

$$\begin{aligned}\Gamma_{(n,0)}^{\text{vib}} = & \quad 3A_{1g} + 3A_{1u} + 3A_{2g} + 3A_{2u} \\ & + 6E_{1g} + 6E_{1u} + 6E_{2g} + 6E_{2u} \\ & + \cdots + 6E_{[(n-1)/2]g} + 6E_{[(n-1)/2]u} \quad (n = \text{odd integer}),\end{aligned}\quad (8)$$

while zigzag nanotubes with even n , are described by the D_{nh} point group and have symmetries:

$$\begin{aligned}\Gamma_{(n,0)}^{\text{vib}} = & \quad 3A_{1g} + 3A_{1u} + 3A_{2g} + 3A_{2u} \\ & + 3B_{1g} + 3B_{1u} + 3B_{2g} + 3B_{2u} \\ & + 6E_{1g} + 6E_{1u} + 6E_{2g} + 6E_{2u} \\ & + \cdots + 6E_{[(n-2)/2]g} + 6E_{[(n-2)/2]u} \quad (n = \text{even integer}).\end{aligned}\quad (9)$$

Since the basic symmetry operations for chiral nanotubes (n, m) involve both rotations and translations, these nanotubes are described by a non-symmorphic space group, in contrast to armchair and zigzag nanotubes for which the translations are decoupled from the rotations, so that these nanotubes are described by symmorphic space groups. Chiral nanotubes follow the point group C_j where $j = (N/2 - 1)$, and the symmetries of the vibrational modes for chiral nanotubes are given by:

$$\Gamma_N^{\text{vib}} = 6A + 6B + 6E_1 + 6E_2 + \cdots + 6E_{N/2-1}, \quad (10)$$

in which the number of hexagons in the 1D unit cell is given by Eq. (3).

For all symmetry types, carbon nanotubes have four modes for which ($\omega \rightarrow 0$) as ($k \rightarrow 0$), and these modes include a mode which describes the rigid rotation of the carbon atoms about the cylindrical axis and has A_{2g} (A) symmetry. The rigid translation mode along the cylinder axis has A_{2u} (A) symmetry, while the rigid translations along the directions perpendicular to this axis have E_{1u} (E_1) symmetry. Here the irreducible representations A_{2g} , A_{2u} and E_{1u} pertain to the groups D_{nh} and D_{nd} , while A and

TABLE 1. Symmetries of Raman-active and IR-active modes for carbon nanotubes [77].

Nanotube structure	point group	Raman-active modes	IR-active modes
armchair (n, n) n even	D_{nh}	$4A_{1g} + 4E_{1g} + 8E_{2g}$	$A_{2u} + 7E_{1u}$
armchair (n, n) n odd	D_{nd}	$3A_{1g} + 6E_{1g} + 6E_{2g}$	$2A_{2u} + 5E_{1u}$
zigzag $(n, 0)$ n even	D_{nh}	$3A_{1g} + 6E_{1g} + 6E_{2g}$	$2A_{2u} + 5E_{1u}$
zigzag $(n, 0)$ n odd	D_{nd}	$3A_{1g} + 6E_{1g} + 6E_{2g}$	$2A_{2u} + 5E_{1u}$
chiral (n, m) $n \neq m \neq 0$	C_N	$4A + 5E_1 + 6E_2$	$4A + 5E_1$

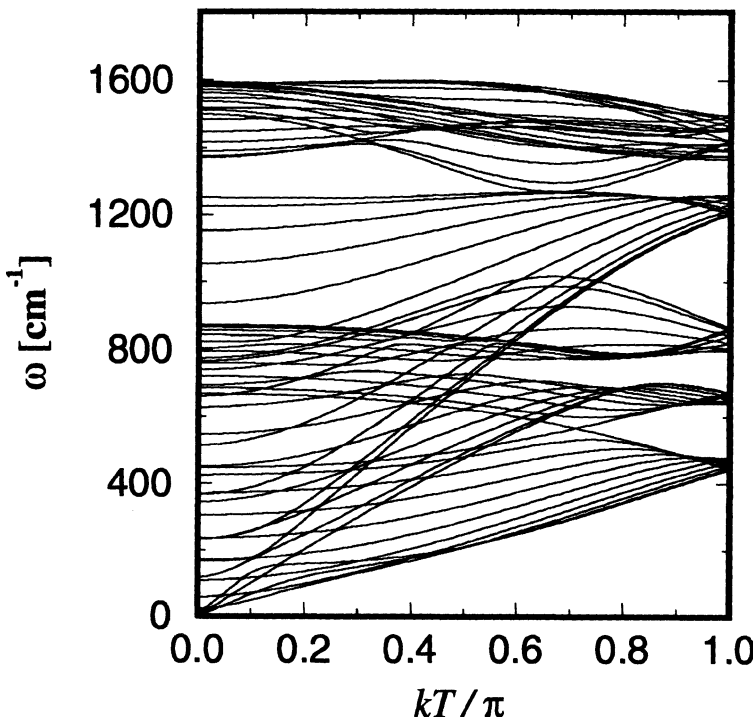


Figure 15. Phonon dispersion relations for a $(10,10)$ armchair carbon nanotube which is capped by a hemisphere of the icosahedral C_{240} fullerene. For the $(10,10)$ nanotube, $N = 20$, and there are 120 vibrational degrees of freedom giving rise to 72 terms in Eq. (7). Of these, 16 are Raman-active ($4A_{1g} + 4E_{1g} + 8E_{2g}$) at the Γ -point ($k = 0$), 8 are infrared-active ($A_{1u} + 7E_{1u}$), three have zero frequencies ($A_{2g} + A_{2u} + E_{1u}$) at $k = 0$, and 45 are optically silent [35].

E_1 pertain to the group C_j ($j = N/2 - 1$). We thus see that the 4 modes with ($\omega \rightarrow 0$) as ($k \rightarrow 0$) belong to three irreducible representations, one of which (E_{1u} or E_1) is two-fold degenerate.

Although the number of vibrational modes increases as the diameter of the carbon nanotube increases, the number of Raman-active and infrared-active modes remains constant for each symmetry type, as given by Eqs. (8), (9), and (10), and explained below. The Raman-active modes transform according to the A_{1g} , E_{1g} , or E_{2g} irreducible representations for groups D_{nh} and D_{nd} , and according to A , E_1 and E_2 for the group C_j ($j = N/2 - 1$). Correspondingly, the infrared-active modes transform as A_{2u} or E_{1u} for groups D_{nh} and D_{nd} , and according to A , and E_1 for the chiral nanotubes. A summary of the number of modes that are Raman-active and infrared-active and their symmetry type is given in Table 1.

The calculated phonon dispersion relations $\omega(k)$ for a (10,10) armchair carbon nanotube based on zone folding of a graphene sheet are given in Fig. 15 [35, 74]. For the $N = 20$ hexagons of carbon atoms per circumferential strip, we have 120 vibrational degrees of freedom, but because of mode degeneracies, there are only 72 distinct optical phonon branches of which 24 modes are non-degenerate and 48 are doubly degenerate. In the case of the (10, 10) armchair nanotube, D_{10h} is the point symmetry group, and the direct product of the reducible representation of the atomic sites with the representations for x , y , z is decomposed into irreducible representations for the phonon modes, as given by Eq. (7), suitably modified for $n/2$ equal to an odd integer.

The idea of zone folding is applicable to almost all the phonon modes of a carbon nanotube. However, it has been pointed out [73] that zone-folding alone does not always give the correct dispersion relation for a carbon nanotube, especially in the low-frequency region, and some additional physical concepts must be introduced. For example, the out-of-plane tangential acoustic (TA) modes of a graphene sheet shown in Fig. 16(a) on the left do not give zero energy at the Γ point when rolled into a nanotube, as shown on the right. Here, at $k = 0$, all the carbon atoms of the nanotube move radially in an out-of-plane radial acoustic vibration. This corresponds to the radial breathing mode with non-zero frequency [73] as shown in Fig. 16(a) on the right, and is featured prominently in the vibrational spectra of carbon nanotubes. The finite frequency of this mode arises from the curvature of the nanotube [35, 73-76].

On the other hand, when we consider the vibrations of a carbon nanotube in the context of three-dimensional space, we generally expect three acoustic modes which correspond to vibrational motions in the x , y , z directions. However, the two directions which are perpendicular to the nanotube axis do not correspond to any two-dimensional graphite phonon modes. In

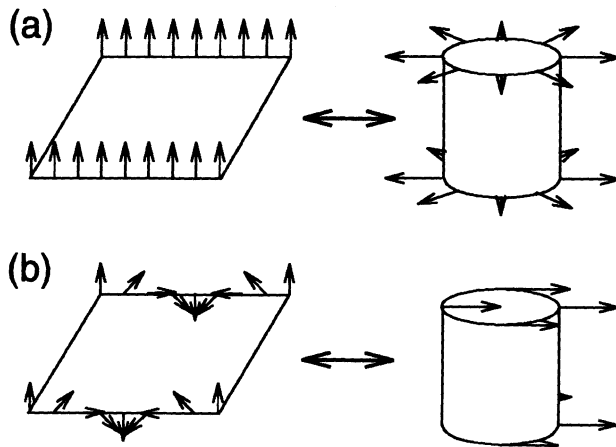


Figure 16. (a) The out-of-plane tangential acoustic modes at $k = 0$ (left) in a single layer of graphite give rise to a radial breathing mode in the carbon nanotube with non-zero frequency (right). (b) An acoustic mode of a carbon nanotube whose vibration is perpendicular to the nanotube axis (right) corresponds to a linear combination of both in-plane and out-of-plane graphite-derived modes (left). These modes do not couple in the case of a single graphite layer, but do couple for the nanotube because of the curvature that is introduced by rolling up the graphene sheet [35].

a graphene sheet, the in-plane and out-of-plane modes are decoupled from each other. However, when the graphene strip is rolled up into a nanotube, the graphite-derived in-plane and out-of-plane modes do couple to each other, as shown on the left-hand side of Fig. 16(b), to form the acoustic mode of the nanotube shown on the right [35]. The issues raised in Fig. 16 are automatically incorporated into the full 3D dynamical matrix used for the calculations of the phonon dispersion relations for carbon nanotubes, such as those given in Fig. 15 for the (10,10) armchair nanotube [35].

Even for armchair and zigzag nanotubes, all of which have relatively small unit cells, there are many phonon branches (as seen in Fig. 15). Because of the large size of the 1D unit cell for chiral nanotubes, they have many degrees of freedom, many more than armchair and zigzag nanotubes. For example, the $(n, m) = (7, 4)$ nanotube has $N = 62$, so that the 1D unit cell has 372 degrees of freedom. The phonon modes will include branches with $6A + 6B + 6E_1 + 6E_2 + \dots + 6E_{30}$ symmetries, 192 branches in all. Of these, only 15 are Raman-active at $k = 0$, while 9 are infrared active, 3 corresponding to the zero-frequency acoustic and rotational modes at $k = 0$, and 162 are optically silent.

Since the number of Raman-active and infrared-active modes for a given symmetry category is independent of nanotube diameter, the dependence of a particular vibrational mode on nanotube diameter can be investigated.

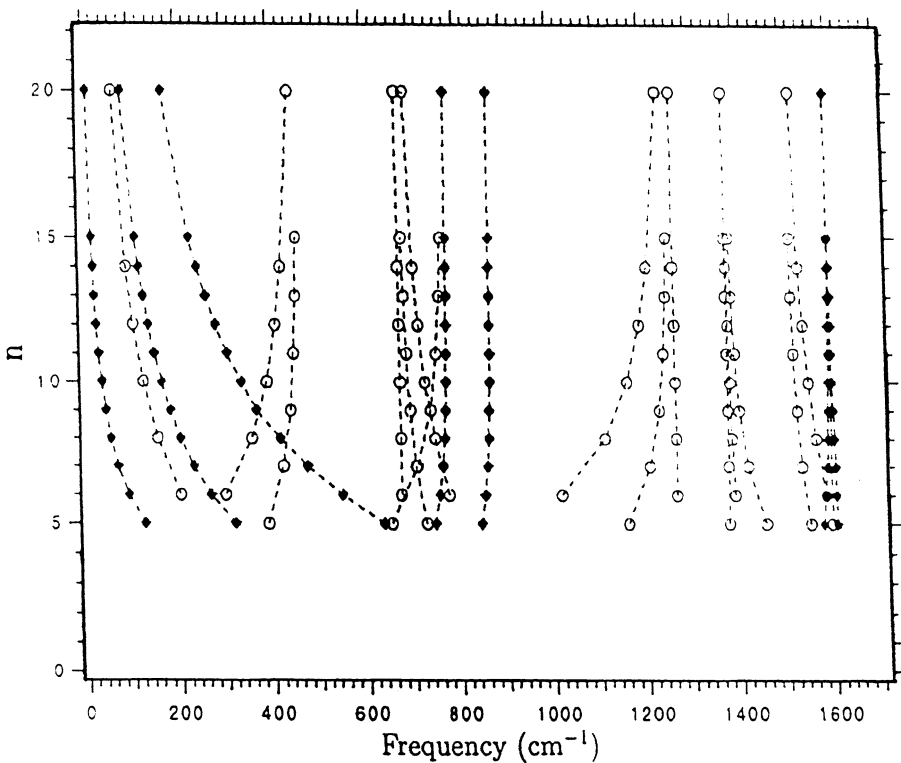


Figure 17. The armchair index n vs. mode frequency for the Raman-active modes of single-wall armchair (n, n) carbon nanotubes [78]. The nanotube diameter can be found from n using Eq. (1).

Many of the mode frequencies and their Raman cross sections are found to be highly sensitive to the nanotube diameter, while others are not. Figure 17 shows the dependence of the frequency of the Raman-active modes on the nanotube diameter for armchair nanotubes, expressed in terms of their (n, n) indices [79]. Here it is seen that the A_{1g} mode, which occurs at about 165 cm^{-1} for a (10,10) nanotube, is strongly dependent on nanotube diameter, while the modes near 1580 cm^{-1} are not. A similar diagram can be constructed for the infrared-active modes for the armchair nanotubes, and also for Raman and infrared-active modes for zigzag and chiral nanotubes [25, 79]. The calculated diameter dependence of the frequency of the A_{1g} radial breathing mode for an isolated single wall nanotube is shown in Fig. 18, where we note that the A_{1g} breathing mode frequency does not depend on nanotube chirality since all carbon atoms move in phase for the radial breathing mode. The normal mode displacements for the most important Raman-active modes are shown in Fig. 19.

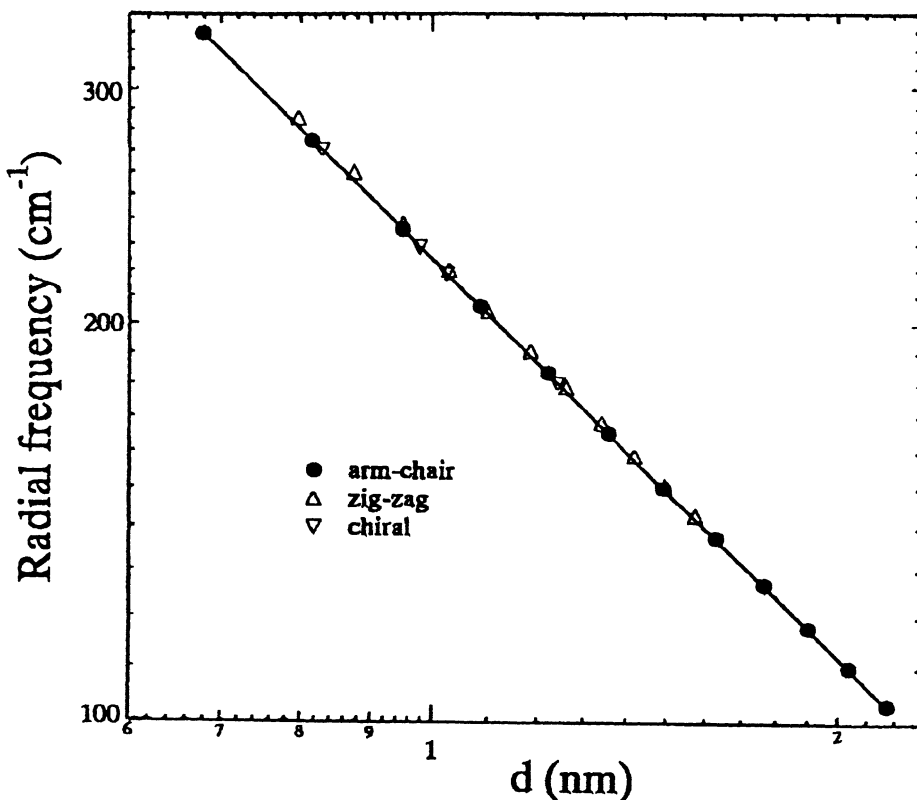


Figure 18. Calculated dependence of the frequency of the A_{1g} radial breathing mode on nanotube diameter d_t plotted on a log-log plot. This plot is for isolated single wall carbon nanotubes.

However, almost all published Raman spectra to date have been on bundles of hundreds of single wall nanotubes, which have been shown to be organized into a triangular lattice, where the van der Waals nanotube-nanotube interactions cannot be completely neglected. Recently, the effect of these interactions on the radial breathing mode frequency has been considered within the framework of the Generalized Tight Binding Molecular Dynamics (GTBMD) scheme, which allows structural relaxation of tube walls in contact within the bundle [80]. The GTBMD results show that for bundles of nanotubes having individual tubes with diameters in the range $0.7 < d_t < 1.5$ nm, the simple $1/d_t$ frequency dependence of the radial breathing mode frequency that was derived for isolated nanotubes can be approximately amended by the addition of a constant upshift of ~ 14 cm $^{-1}$, independent of d_t . The upshift is the result of an additional tube-wall restoring force due to next-neighbor, tube-tube interactions. This frequency up-

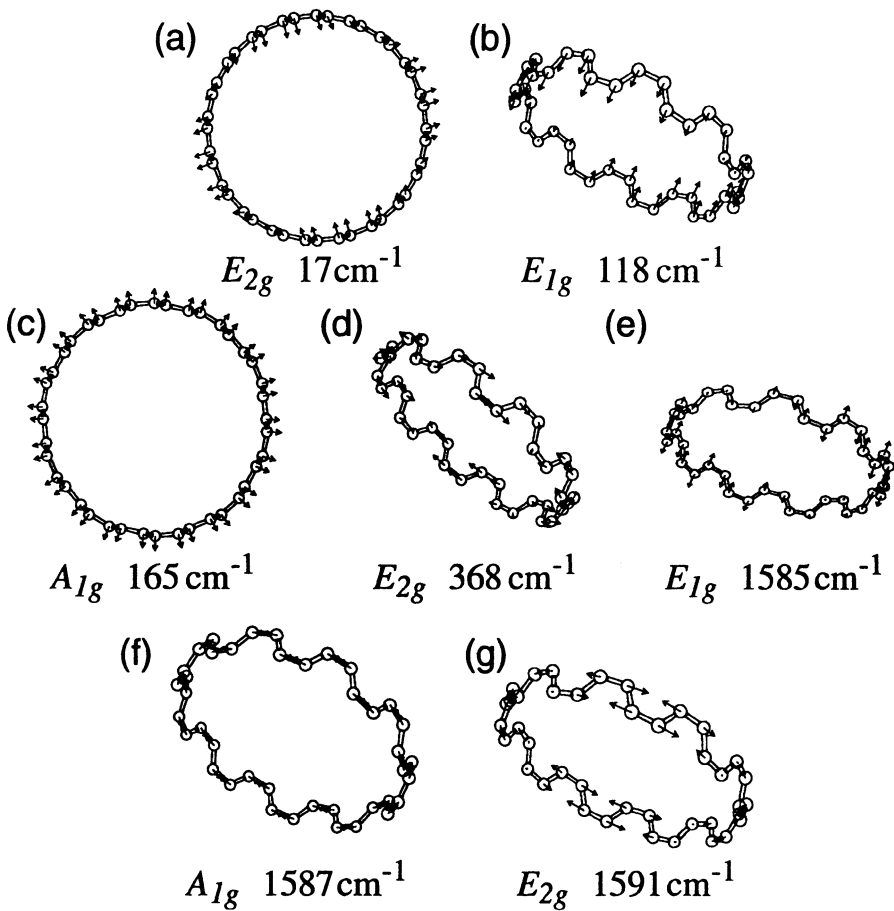


Figure 19. The calculated Raman mode atomic displacements, frequencies, and symmetries for selected normal modes for the (10,10) nanotube modes. The symmetry and the frequencies for these modes are not strongly dependent on the chirality of the nanotube. In the figure, we show the displacements for only one of the two modes in the doubly degenerate E_{1g} , and E_{2g} modes [35].

shift corresponds to an approximately 7% increase in the individual single wall nanotubes diameter inferred from the experimental radial breathing mode frequency, or a shift that is comparable to the diameter change between a (10,10) and a (11,11) nanotube. Further calculations should be done to confirm the value for this interaction term, since the breathing mode band provides a convenient means for estimating the tube diameter distribution as long as several spectra with different laser excitation frequencies are collected [15, 81-86].

1.6. RAMAN SPECTRA

Raman spectroscopy provides a particularly valuable tool for examining the mode frequencies of carbon nanotubes with specific diameters and thereby evaluating the merits of various theoretical models for the 1D phonon dispersion relations for carbon nanotubes. This technique is also being used to characterize nanotube samples in terms of the diameter distribution of the nanotubes in the sample, and for studying the 1D electron density of states in resonant Raman experiments through the electron-phonon coupling mechanism [78].

Most of the early experiments on the vibrational spectra of carbon nanotubes were carried out on multi-wall carbon nanotubes, which were too large in diameter to observe detailed quantum effects associated with the 1D dispersion relations discussed above [87, 88]. The first Raman study to show a clear signature for single-wall carbon nanotubes [89] was carried out on samples containing only a small concentration of single-wall nanotubes, and having a wide distribution of diameters and chiralities, so that only features pertinent to phonon modes near 1580 cm^{-1} , which are only weakly dependent on nanotube diameter, could be observed [89].

The first definitive study of the Raman spectrum of single-wall carbon nanotubes was carried out on a sample containing several ropes of single-wall carbon nanotubes with a narrow diameter distribution in the $1.2\text{--}1.4\text{ nm}$ range, and prepared by laser vaporization techniques [6]. The Raman spectrum taken on this sample at a 514.5 nm laser excitation wavelength is shown in Fig. 20 [78]. Prominent in this spectrum are a number of features near 1580 cm^{-1} (see inset to Fig. 20), and a strong feature at $\sim 186\text{ cm}^{-1}$. From Fig. 17, we see that there are three mode frequencies A_{1g} , E_{1g} and E_{2g} for armchair nanotubes near 1580 cm^{-1} , each mode frequency being almost independent of nanotube diameter. A similar behavior is found for the Raman band near 1580 cm^{-1} for zigzag and chiral nanotubes. The atomic displacements associated with the normal modes near $\sim 186\text{ cm}^{-1}$ and $\sim 1580\text{ cm}^{-1}$ for a $(10,10)$ nanotube are shown in Fig. 19 [35]. In contrast to the high-frequency band near 1580 cm^{-1} , the feature near $\sim 186\text{ cm}^{-1}$, which is identified with an A_{1g} radial breathing mode, is strongly dependent on the nanotube diameter, as shown in Fig. 17. Calculations [74, 75] show that the intensities for these radial breathing and tangential modes are expected to dominate the Raman spectra, in agreement with experiment. The other Raman-active modes (see Fig. 17) are predicted to have low Raman cross sections, also in agreement with experiment (Fig. 20). Calculations further predict that the relative intensity of the weaker Raman-active features in the experimental spectra can be increased by making measurements on carbon nanotubes of small length

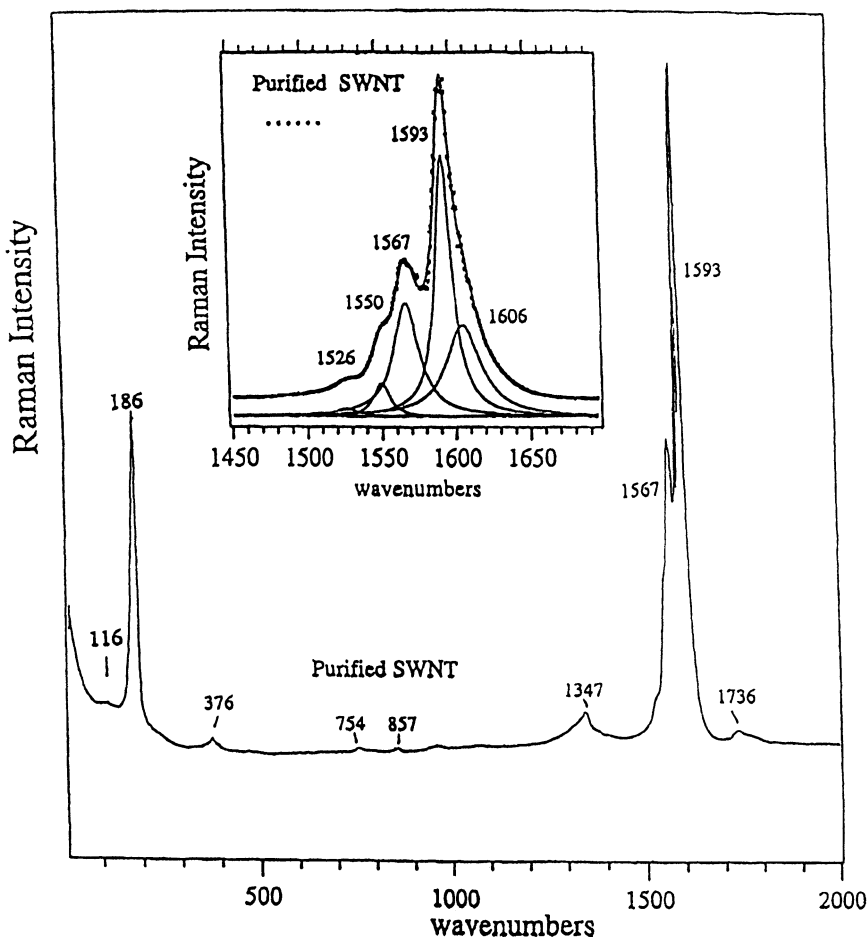


Figure 20. Experimental Raman spectrum taken with 514.5 nm laser excitation from a sample consisting primarily of single-wall nanotubes with diameters d_t near that of the (10,10) nanotube ($d_t = 1.38 \text{ nm}$) [78].

[90].

Quantum effects are observed in the Raman spectra of single-wall carbon nanotubes through the resonant Raman enhancement effect, which is seen experimentally by measuring the Raman spectra at a number of laser excitation energies, as shown in Fig. 21. Because of this strong resonant enhancement effect, only a small concentration of single wall nanotubes in a sample containing other carbon forms can give rise to spectral features showing the characteristic sharp doublet structure in the 1570–1600 cm⁻¹ range [89]. Resonant enhancement in the Raman scattering intensity from

carbon nanotubes occurs when the laser excitation frequency corresponds to a transition between the sharp features in the one-dimensional electronic density of states (see Fig. 9) of the carbon nanotubes, as shown in Fig. 22 for (8,8), (9,9), (10,10), (11,11), and (12,12) armchair nanotubes and for (14,0), (15,0), (16,0), (17,0), and (18,0) zigzag nanotubes [78]. Since the energies of these sharp features in the 1D electronic density of states are strongly dependent on the nanotube diameter, a change in the laser frequency brings into resonance a carbon nanotube with a different diameter. For example, the model calculation in Fig. 22 shows that the (10,10) armchair nanotube would be expected to be resonant at a laser frequency of 1.9 eV, while the (9,9) nanotube would be resonant at 2.1 eV. However, armchair nanotubes with different diameters have different vibrational frequencies for the A_{1g} breathing mode (see Figs. 17 and 18). By comparing

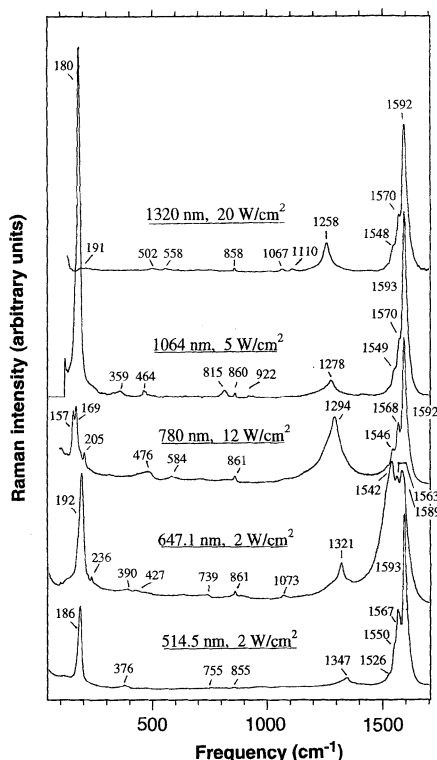


Figure 21. Experimental room temperature Raman spectra for purified single-wall carbon nanotubes excited at five different laser excitation wavelengths. The laser wavelength and power density for each spectrum are indicated, as are the vibrational frequencies (in cm^{-1}) [78]. The equivalent photon energies for the laser excitation are: 1320 nm \rightarrow 0.94 eV; 1064 nm \rightarrow 1.17 eV; 780 nm \rightarrow 1.58 eV; 647.1 nm \rightarrow 1.92 eV; 514.5 nm \rightarrow 2.41 eV.

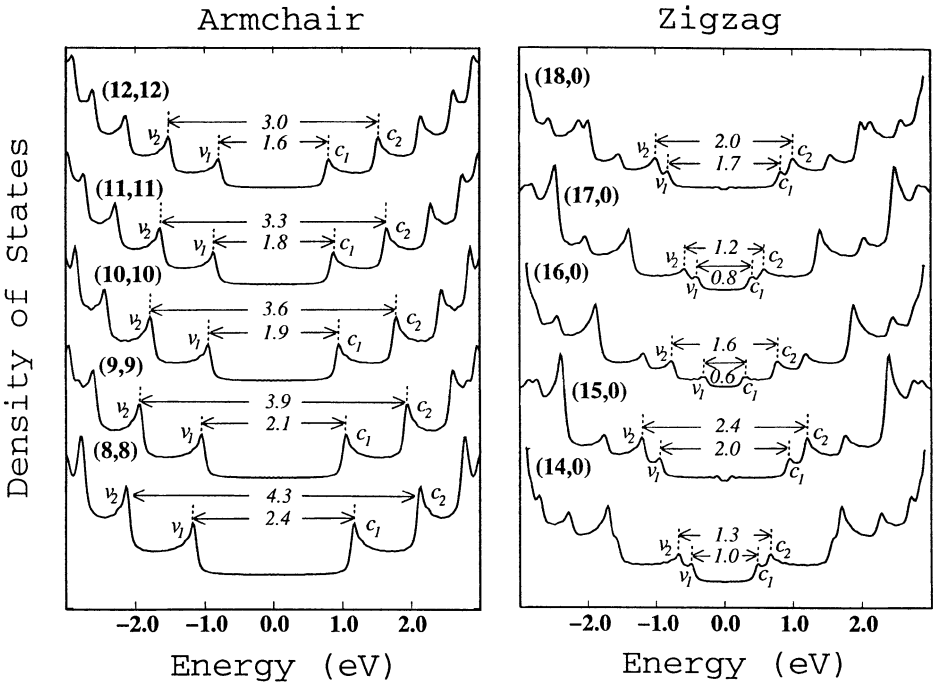


Figure 22. Electronic 1D density of states (DOS) calculated with a tight binding model for (8,8), (9,9), (10,10), (11,11), and (12,12) armchair nanotubes and for (14,0), (15,0), (16,0), (17,0), and (18,0) zigzag nanotubes. Wave vector conserving optical transitions can occur between mirror image spikes in the 1D density of states, i.e., $v_1 \rightarrow c_1$ and $v_2 \rightarrow c_2$, etc., and these optical transitions are given in the figure in units of eV. These transitions are denoted in the text by E_{11} , E_{22} , etc. and are responsible for the resonant Raman effect shown in Fig. 21 [91].

the various Raman spectra in Fig. 21 at different laser excitation energies, we see large differences in the vibrational frequencies and intensities of the strong A_{1g} mode, consistent with a resonant Raman effect involving nanotubes of different diameters. The dependence of the Raman intensity and line shape of the radial breathing mode on laser excitation frequency (see Fig. 21) is also consistent with a resonant Raman scattering mechanism. These experimental observations provided the first clear confirmation for the theoretical predictions about the singularities in the 1D electronic density of states of carbon nanotubes, and this confirmation was soon corroborated by a more direct measurement of the 1D electronic density of states by STM/STS spectroscopy [21, 22]. Because of the sensitivity of the radial breathing mode feature to laser excitation energy, the Raman technique has been used to provide information about the diameter distribution in carbon nanotube samples prepared with different catalysts, growth temperatures

and other process variables [7, 81-83].

The Raman band between $1400\text{--}1700\text{ cm}^{-1}$, associated with the tangential C-C stretching modes of the single-wall carbon nanotubes, obtained with different laser lines over a wide energy range ($0.94 \leq E_{\text{laser}} \leq 3.05\text{ eV}$) [18, 78, 92, 93] is shown in Fig. 23. Here we see that the spectra obtained for $E_{\text{laser}} < 1.7\text{ eV}$ or $E_{\text{laser}} > 2.2\text{ eV}$ are quite similar, and can all be fit by essentially the same set of Lorentzian oscillators. In contrast, the spectra obtained in the narrow range $1.7 \leq E_{\text{laser}} \leq 2.2\text{ eV}$ are qualitatively different, showing bands that are broader and centered at lower frequencies. The inset to Fig. 23 shows low-resolution Raman spectra between 1300 and 2800 cm^{-1} using three laser energies in the transition region between the two regimes [93]. The spectra show that the intensity of the second-order band at 2700 cm^{-1} is almost independent of E_{laser} , whereas the intensity of the tangential band is enhanced when E_{laser} approaches 2 eV . Analysis of these spectra indicate that the spectral features in Fig. 23 for $E_{\text{laser}} < 1.7\text{ eV}$ and $E_{\text{laser}} > 2.2\text{ eV}$ are associated with semiconducting carbon nanotubes with the maximum Raman intensity occurring at 1593 cm^{-1} , while the Raman spectra for $1.7 \leq E_{\text{laser}} \leq 2.2\text{ eV}$ with a Raman peak intensity at 1540 cm^{-1} are associated with metallic nanotubes.

For a metallic tube with a given diameter d_t , the enhancement of its Raman peaks will occur every time the incident or scattered photon is in resonance with the energy separation between the highest valence subband $E_{v_1}(d_t)$ and the lowest conduction subband $E_{c_1}(d_t)$, so that $E_{11}(d_t) = E_{c_1}(d_t) - E_{v_1}(d_t)$ [74]. Since the sample contains metallic nanotubes with diameters in the range $1.1\text{--}1.6\text{ nm}$ (see inset of Fig. 24), the overall enhancement of the intensity of the Raman modes is given by the sum of the contributions of each individual nanotube with a given diameter d_t , weighted by the distribution of diameters. The Raman cross section $I(E_{\text{laser}})$ can then be written as [94]:

$$\begin{aligned} I(E_{\text{laser}}) = & \sum_{d_t} A \exp \left[\frac{-(d_t - d_0)^2}{\Delta d_t^2 / 4} \right] \\ & \times [(E_{11}(d_t) - E_{\text{laser}})^2 + \gamma_e^2 / 4]^{-1} \\ & \times [(E_{11}(d_t) - E_{\text{laser}} + E_{\text{phonon}})^2 + \gamma_e^2 / 4]^{-1}, \end{aligned} \quad (11)$$

where d_0 and Δd_t are the center and the width of the Gaussian distribution of nanotube diameters, $a_{\text{C-C}}$ is the carbon-carbon distance, γ_0 is the electronic overlap integral, E_{phonon} is the average energy (0.197 eV) of the tangential phonons, the damping factor γ_e accounts for the width of the singularities in the electronic DOS and the lifetime of the excited state [74],

and the diameter dependence of $E_{11}(d_t)$ is given by [47, 62]

$$E_{11}(d_t) = \frac{6a_{C-C}\gamma_0}{d_t}. \quad (12)$$

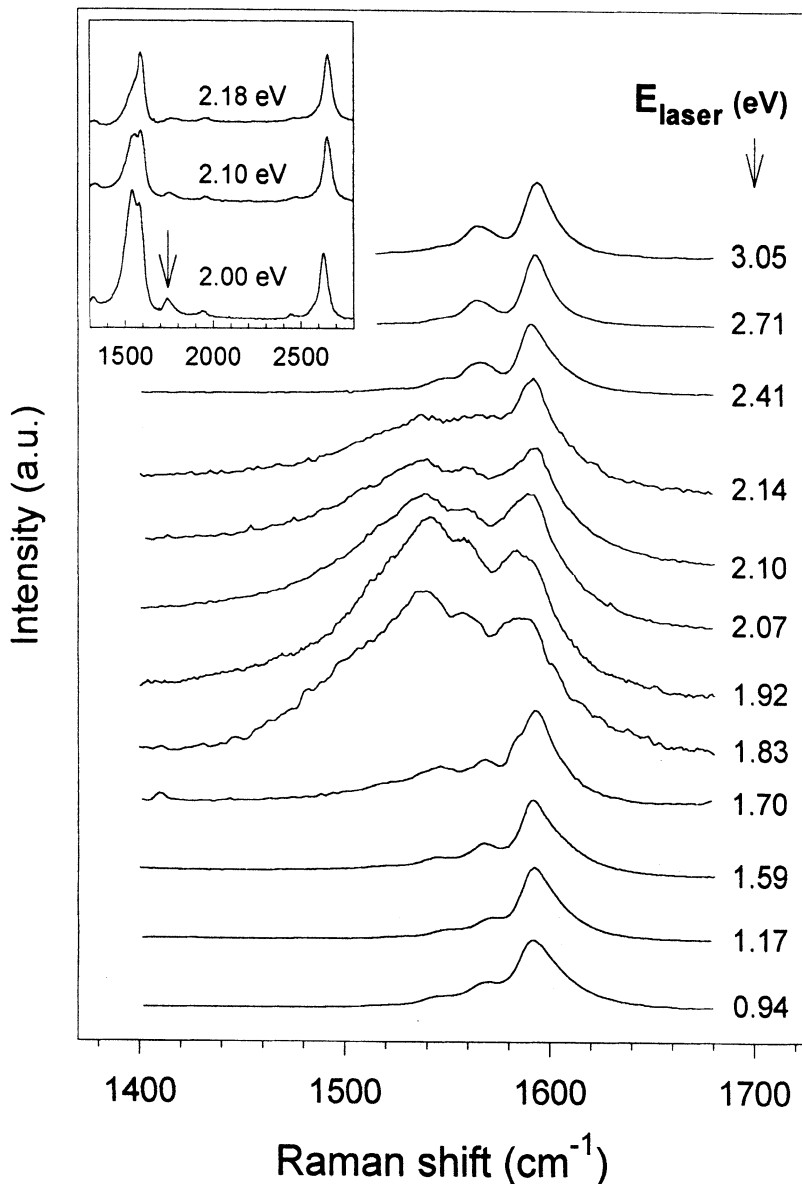


Figure 23. Raman spectra of the tangential modes of carbon nanotubes obtained with several different laser lines. The inset shows low-resolution Raman spectra between 1300 and 2800 cm^{-1} in the range of laser energies 2.00–2.18 eV where the metallic nanotubes are dominant [93].

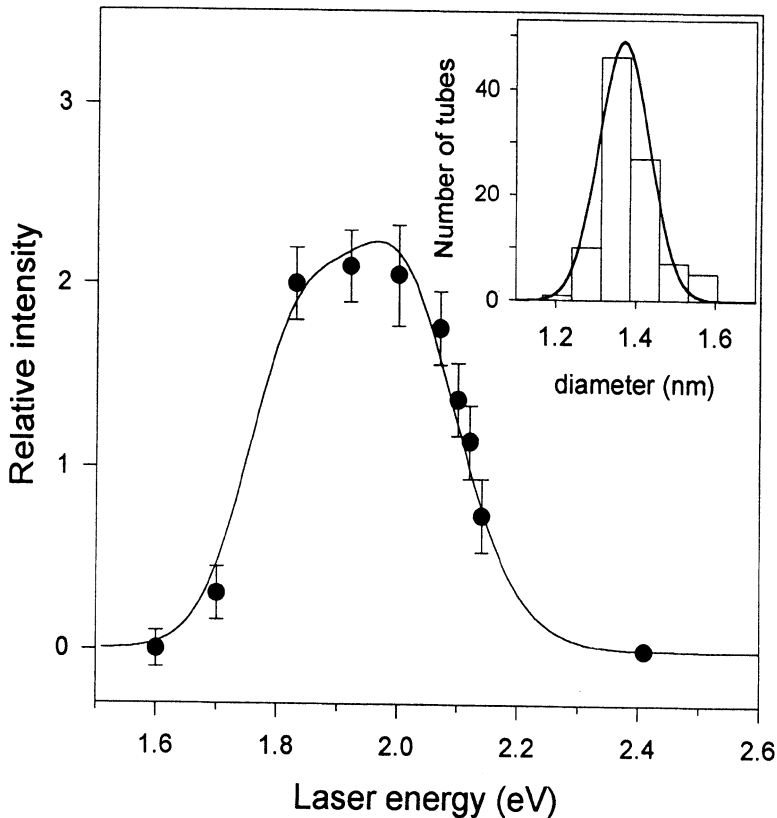


Figure 24. The solid circles represent the intensity ratio of the Raman peaks at 1540 and 1593 cm^{-1} , and the solid curve represents the fit to the experimental data using Eqs. (11) and (12) [93]. The inset shows the distribution of diameters measured by TEM [78] and the Gaussian fit to the diameter distribution data [93].

The best fit of Eq. (11) to the plot of the intensity ratio I_{1540}/I_{1593} vs. E_{laser} measurements in Fig. 24 using $d_0 = 1.37 \text{ nm}$ and $\Delta d_t = 0.18 \text{ nm}$ from the TEM measurements, yields $\gamma_0 = 2.95 \pm 0.05 \text{ eV}$, $\gamma_e = 0.04 \pm 0.02 \text{ eV}$, a full width of the distribution $\Delta E_{11}(d_t) = 0.24 \text{ eV}$, and a mean value for the energy separation $\langle E_{11}(d_t) \rangle = 1.84 \text{ eV}$ which are in good agreement with the direct measurements of $E_{11}(d_t)$ by STS [21] and with Electron Energy Loss Spectroscopy (EELS) experiments [95].

Raman spectra have also been taken on doped single-wall carbon nanotube ropes [67, 96, 97]. These spectra show effects similar to the effect of alkali metal and halogen intercalation into graphite [97], exhibiting upshifts in the frequency associated with the donation of electrons from graphite to the halogens in the case of acceptors, and downshifts in mode frequencies associated with donor charge transfer to graphite in the case of alkali metal intercalation (see Fig. 25) [66, 72, 96, 98, 99]. To date, Raman scattering

studies have only been carried out on as-prepared (and unpurified) material taken directly from the synthesis chamber and exposed to the following reactants: (donors) Li [98], K and Rb [96]; (acceptors) sulfuric acid (H_2SO_4) [99]; Br_2 [96], iodine (I_2) vapor [96], and molten iodine [66], though iodine does not form a graphite intercalation compound (GIC). The presumption for all single-wall carbon nanotube charge transfer processes is that the dopant resides as ions (and also possibly as neutral atoms) in the interstitial channels between the tubes in the triangular nanotube lattice. This has yet to be confirmed by x-ray diffraction, or other structural probes.

Both the radial and tangential Raman-active nanotube modes have been observed to upshift or downshift significantly with doping. Since the sign of the shift in nanotubes is usually consistent with earlier studies of intercalation in GICs and C_{60} , the shift has therefore been interpreted [96] in terms of C-C bond expansion or contraction. For example, Br_2 intercalation makes the tangential modes *upshift* by 24 cm^{-1} . In the case of the donor dopants (K, Rb), the tangential vibrational bands *downshift*, and the spectra are remarkably similar, suggesting that under the experimental conditions used, both reactions proceed to the same endpoint stoichiome-

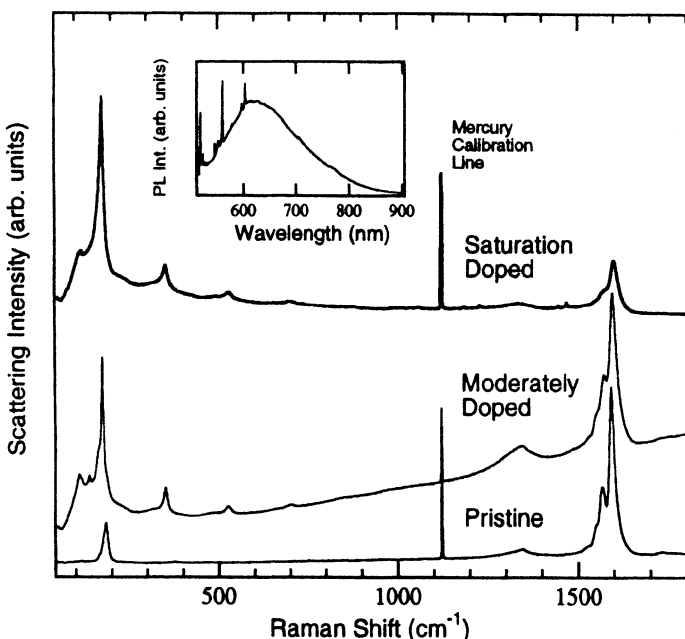


Figure 25. Raman spectra of pristine, moderately I-doped, and saturation I-doped single-wall nanotube samples ($T = 300\text{ K}$, 514.5 nm laser excitation) where molten I_2 is the dopant. The insert shows the photoluminescence spectrum due to the intercalated polyiodide chains in the moderately doped sample where sharp Raman lines are superimposed on the broad PL spectrum [66].

try. The highest-frequency tangential modes in the K and Rb intercalate nanotube Raman spectra were fit to a Breit-Wigner-Fano line shape, similar to that found for the first stage MC_8 GICs ($M = \text{K}, \text{Rb}, \text{Cs}$), although the coupling constant ($1/q$) is a factor of three lower than observed in GICs [100], thereby leading to a narrower linewidth for the doped nanotubes. A variety of other Raman features in the region $900 - 1400 \text{ cm}^{-1}$ were also observed for the donor intercalated nanotubes, but no specific assignments were made, since the corresponding modes in the pristine sample were not observed.

Charge transfer reactions of as-prepared bundles of single-wall carbon nanotubes with molten iodine (see Fig. 25) produced a much more dramatic effect on the Raman spectrum than was observed when the reaction was carried out in iodine vapor [66]. The Raman spectra clearly showed the effects of a charge transfer reaction with the single wall nanotube bundles to be reversible and uniform, producing an air stable compound of an approximate stoichiometry C_{12}I . The Raman spectra in Fig. 25 for undoped (pristine), moderately I-doped, and saturation I-doped single-wall nanotube bundles [66, 72] show a low-frequency region which is rich in structure, identified with the presence of intercalated charged polyiodide chains (I_3^- and I_5^-). No Raman evidence for neutral I_2 (215 cm^{-1}) was found in the nanotube samples. Saturation doping was found to convert I_3^- observed in the moderately doped material into I_5^- . Analysis of these data showed that intercalation *downshifts* the radial band from 186 to 175 cm^{-1} , while the tangential band is *upshifted* by 8 cm^{-1} from 1593 to 1601 cm^{-1} . The radial mode downshift may be due to a coupling of the tube wall to the heavy iodine chains, while the small tangential mode upshift (8 cm^{-1}) compared to the 21 cm^{-1} upshift in Br_2 is attributed to the iodine chains being only singly ionized. If all the iodine was in the form of I_5^- in the C_{12}I compound, we might write the formula as $\text{C}_{60}^+(\text{I}_5)^-$, which is equivalent to one hole per 60 C-atoms, and we therefore find an upshift of 8 cm^{-1} per additional hole per 60 C-atoms in the single-wall nanotubes (or 480 cm^{-1} per hole per C-atom). This shift can be compared to that of 6 cm^{-1} per added electron in M-doped C_{60} (or 360 cm^{-1} per electron per C-atom).

In situ Raman scattering studies, performed during the electrochemical anodic oxidation of single-wall carbon nanotube bundles in sulfuric acid [99], are of special interest, and can be directly compared with similar studies on H_2SO_4 GICs [101]. In the case of the nanotubes, a rapid spontaneous shift of $\sim 15 \text{ cm}^{-1}$ in the tangential Raman modes was observed under open circuit conditions which was not observed in the GIC system. In the H_2SO_4 single wall nanotube study, a direct measure was obtained for the charge transfer effect on the tangential mode frequency, i.e., 320 cm^{-1} per hole per C-atom, in reasonable agreement with values discussed above for M-doped

C₆₀.

1.7. MECHANICAL PROPERTIES

The elastic properties of fullerene-related nanotubes have been discussed both theoretically and experimentally [102-104]. Direct observations, mostly using high-resolution TEM, have shown that small diameter single-wall carbon nanotubes are remarkably flexible, and bend into curved arcs with radii of curvature as small as 20 nm. This flexibility suggests excellent mechanical properties, consistent with the high tensile strength and bulk modulus of commercial and research-grade vapor grown carbon fibers [102]. As shown in Fig. 26, even relatively large diameter (\sim 10 nm) carbon nanotubes grown from the vapor phase can bend, twist, and kink without fracturing [105, 106]. The basic mechanical properties of the nanotubes are

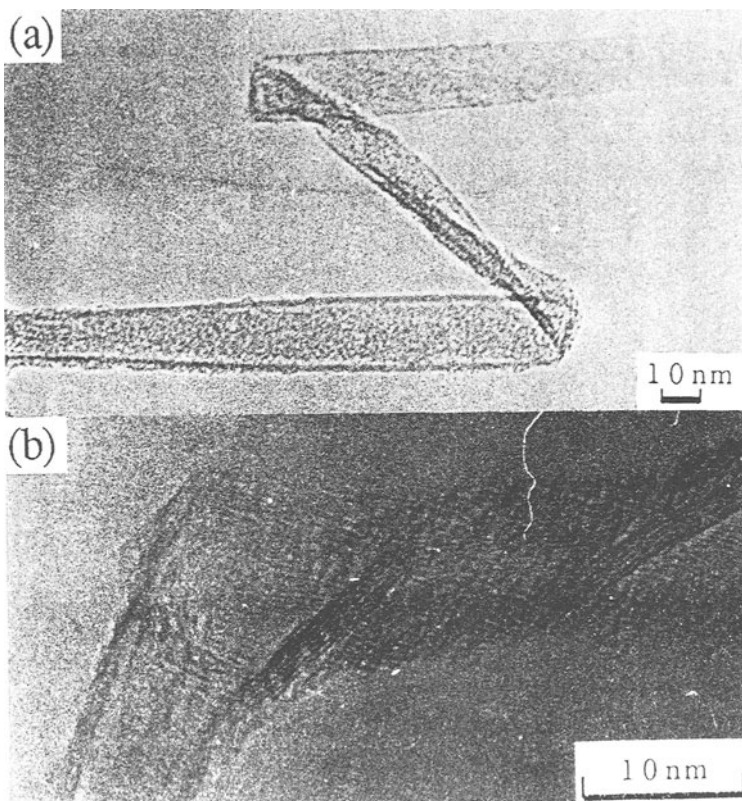


Figure 26. High-resolution TEM images of bent and twisted carbon nanotubes. The length scales for these images are indicated [105].

very different from those of conventional PAN-based and vapor-grown carbon fibers, which are much more fragile and are easily broken when bent or twisted. It is of interest to note that when bent or twisted, the nanotubes appear to flatten in cross section, especially single wall nanotubes with larger diameters [104, 106, 107]. Single-wall carbon nanotubes are also remarkable regarding their mechanical properties under compression. Whereas carbon fibers fracture easily under compression, carbon nanotubes form kink-like ridges under compression and these ridges can relax elastically when the stress is released. Extreme hardness was also found for bundles of carbon nanotubes, exceeding that of the toughest alloys used as substrates [103]. Theoretical studies indicate that for $d_t < 2 \text{ nm}$ the effect of the strain energy exceeds that of the room temperature thermal energy [108, 109], so that it is only at small nanotube diameters that the strain energy associated with nanotube curvature is important. Calculations for the energetics of the stretching and compression of multi-wall nanotubes show good agreement with an elastic continuum model based on the elastic constant of C_{11} for graphite [110-112].

The large value measured for the Young's modulus [1.8 TPa (terapascal)] [109, 113] accounts for the straightness of small diameter nanotubes in TEM micrographs [107]. Theoretical simulations using 3-body potentials [109] have yielded values as high as 5 TPa for the Young's modulus (Y) of an individual single wall nanotube, more than the calculated in-plane elastic modulus of graphite (1.06 TPa). Furthermore, these same simulations report a tensile strain to failure as high as 40% [109]. Raman spectroscopy has also been used indirectly to obtain a value of Young's modulus in both single wall [114] and multiwall nanotubes [115] by measuring the shift with strain of the frequency of the second-order Raman band referred to as the D^* band, usually found in graphitic carbons and nanotubes in the region $2600\text{--}2700\text{ cm}^{-1}$. The frequency shift with strain has been calibrated in terms of applying stress to carbon fibers, which were found to exhibit a linear relationship between the peak shift and the applied strain. These Raman measurements to determine Y were performed on nanotubes dispersed into epoxy (at low loading), using cooling-induced compressive strain [114]. Values of Y from Raman measurements on both single wall [114] and multiwall nanotubes [115] are in good agreement with prior measurements of Y based on observing the macroscopic vibrations of the whole tube [113]. In a second, independent study, quite different transfer of the applied load to multiwall nanotubes was observed under tension and compression [115]. The poor transfer under tension was attributed to either poor bonding of the epoxy to the outermost shell of the multiwall tube, or to the ineffective transfer of the load that is applied to the outer shell but then must be transferred to the internal shells of the multiwall tube. This poor trans-

fer of a load from the outer to inner tube shells in multiwall nanotubes raises some doubt that they will be suitable for strength enhancing fillers in composites.

Very low expansion coefficients are also expected tangential to the nanotube surface, consistent with the anisotropic and anomalous thermal expansion coefficient for graphite which is small and negative in-plane, and large and positive along the *c*-axis. In summary, single-wall carbon nanotubes are believed to possess many of the desirable mechanical properties of carbon fibers, but, in addition, single-wall carbon nanotubes have a number of other desirable properties with regard to bending them into loops, cross-sectional distortions, twisting distortions, and elongation and compression without fracture.

1.8. APPLICATIONS

Many research opportunities exist for the controlled manipulation of structures of nm dimensions. Advances made in the characterization and manipulation of carbon nanotubes should therefore have a substantial general impact on the science and technology of nanostructures. The exceptionally high modulus and strength of thin multi-wall carbon nanotubes can be used in the manipulation of carbon nanotubes and other nanostructures [104, 109, 116].

The caps of carbon nanotubes were shown to be more chemically reactive than the cylindrical sections [117], and the caps have been shown to be highly efficient electron emitters [118-121]. It is interesting to point out the successful fabrication of a lattice of tiny catalyst nanoparticles on a silicon wafer, and from this array of catalyst particles arrays of single-wall carbon nanotubes were grown in the vapor phase [121, 122]. While the initial application of this array was for displays, other interesting applications can be envisioned. The electron emission application could be of commercial significance. Therefore, applications of nanotubes for displays and for electron probe tips have been discussed. The ability of carbon nanotubes to retain relatively high gas pressures within their hollow cores suggest another possible area for applications [123]. Carbon nanotubes have been proposed as a flexible starting point for the synthesis of new nano-scale and nano-structured carbides, whereby the carbon nanotube serves as a template for the subsequent formation of carbides. The sandwiching of layers of insulating BN cylinders surrounded by carbon cylinders on either side offers exciting possibilities for electronic applications [38]. By analogy with carbon fibers which are used commercially in composites for structural strengthening and for enhancement of the electrical conductivity, it should also be possible to combine carbon nanotubes with a host poly-

mer (or metal) to produce composites with physical properties that can be tailored to specific applications. The small size of carbon nanotubes allow them to be used in polymer composite materials that can be extruded through an aperture (die) to form shaped objects with enhanced strength and stiffness or enhanced electrical conductivity. Carbon nanotubes can be added to low-viscosity paints that can be sprayed onto a surface, thereby enhancing the electrical conductivity of the coating.

As further research on carbon nanotubes and related materials is carried out, it is expected, because of the unusual properties exhibited by these materials, that other interesting physics and chemistry will be discovered, and that promising applications will be found.

Acknowledgments

We gratefully acknowledge the helpful discussions with Professors J.C. Charlier, Morinobu Endo and Riichiro Saito. We are also in debt to many other colleagues for assistance. The research at MIT is funded by NSF grants DMR-95-10093 and DMR-98-04734. The work at UK was supported by NSF grant OSR-9452895. PCE and AMR were supported by the University of Kentucky Center for Applied Energy Research and the NSF Grant No. EHR-91-08764.

References

1. S. Iijima, *Nature (London)* **354**, 56 (1991).
2. T. W. Ebbesen and P. M. Ajayan, *Nature (London)* **358**, 220 (1992).
3. T. W. Ebbesen, H. Hiura, J. Fujita, Y. Ochiai, S. Matsui, and K. Tanigaki, *Chem. Phys. Lett.* **209**, 83–90 (1993).
4. S. Iijima and T. Ichihashi, *Nature (London)* **363**, 603 (1993).
5. D. S. Bethune, C. H. Kiang, M. S. de Vries, G. Gorman, R. Savoy, J. Vazquez, and R. Beyers, *Nature (London)* **363**, 605 (1993).
6. A. Thess, R. Lee, P. Nikolaev, H. Dai, P. Petit, J. Robert, C. Xu, Y. H. Lee, S. G. Kim, A. G. Rinzler, D. T. Colbert, G. E. Scuseria, D. Tománek, J. E. Fischer, and R. E. Smalley, *Science* **273**, 483–487 (1996).
7. C. Journet, W. K. Maser, P. Bernier, A. Loiseau, M. Lamy de la Chapelle, S. Lefrant, P. Deniard, R. Lee, and J. E. Fischer, *Nature (London)* **388**, 756–758 (1997).
8. M. S. Dresselhaus, G. Dresselhaus, and R. Saito, *Carbon* **33**, 883–891 (1995).
9. M. S. Dresselhaus, G. Dresselhaus, and R. Saito, *Phys. Rev. B* **45**, 6234 (1992).
10. M. Endo, H. Fujiwara, and E. Fukunaga, Meeting of Japanese Carbon Society pages 34–35 (1991) (unpublished).
11. M. Endo, H. Fujiwara, and E. Fukunaga, Second C₆₀ Symposium in Japan pages 101–104 (1992) (unpublished).
12. T. W. Ebbesen, *Annu. Rev. Mater. Sci.* **24**, 235–264 (1994).
13. M. Endo, *CHEMTECH* **18**, 568 (1988).
14. T. Guo, C.-M. Jin, and R. E. Smalley, *Chem. Phys. Lett.* **243**, 49–54 (1995).
15. H. M. Cheng, F. Li, X. Sun, S. D. M. Brown, M. A. Pimenta, A. Marucci, G. Dresselhaus, and M. S. Dresselhaus, *Chem. Phys. Lett.* **289**, 602–610 (1998).

16. J. C. Charlier and J. P. Michenaud, *Phys. Rev. Lett.* **70**, 1858–1861 (1993).
17. J.-C. Charlier, T. W. Ebbesen, and Ph. Lambin, *Phys. Rev. B* **53**, 11108 (1996).
18. A. Kasuya, Y. Sasaki, Y. Saito, K. Tohji, and Y. Nishina, *Phys. Rev. Lett.* **78**, 4434 (1997).
19. H. Kataura, A. Kimura, Y. Maniwa, S. Suzuki, H. Shiromaru, T. Wakabayashi, S. Iijima, and Y. Achiba, unpublished (1997).
20. R. Bacon, *J. Appl. Phys.* **31**, 283–290 (1960).
21. J. W. G. Wildöer, L. C. Venema, A. G. Rinzler, R. E. Smalley, and C. Dekker, *Nature (London)* **391**, 59–62 (1998).
22. T. W. Odom, J. L. Huang, P. Kim, and C. M. Lieber, *Nature (London)* **391**, 62–64 (1998).
23. K. Sattler, *Carbon* **33**, 915–920 (1995).
24. R. Saito, M. Fujita, G. Dresselhaus, and M. S. Dresselhaus, *Appl. Phys. Lett.* **60**, 2204–2206 (1992).
25. M. S. Dresselhaus, G. Dresselhaus, and P. C. Eklund, *Science of Fullerenes and Carbon Nanotubes* (Academic Press, New York, 1996).
26. S. G. Louie. In *Physics and Chemistry of Materials with Low-Dimensional Structures: Fullerene-Based Materials*, edited by Wanda Andreoni, (Kluwer, Dordrecht, 1999) Chapter 9 of this volume.
27. R. Saito, G. Dresselhaus, and M. S. Dresselhaus, *Chem. Phys. Lett.* **195**, 537 (1992).
28. J. W. Mintmire, B. I. Dunlap, and C. T. White, *Phys. Rev. Lett.* **68**, 631–634 (1992).
29. T. Hamada, M. Furuyama, T. Tomioka, and M. Endo, *J. Mater. Res.* **7**, 1178–1188 (1992). *ibid.*, 2612–2620.
30. K. Harigaya, *Chem. Phys. Lett.* **189**, 79 (1992).
31. K. Tanaka, M. Okada, K. Okahara, and T. Yamabe, *Chem. Phys. Lett.* **191**, 469 (1992).
32. R. Saito, M. Fujita, G. Dresselhaus, and M. S. Dresselhaus. In *Electrical, Optical, and Magnetic Properties of Organic Solid State Materials, MRS Symposia Proceedings, Boston*, edited by L. Y. Chiang, A. F. Garito, and D. J. Sandman (Materials Research Society Press, Pittsburgh, 1992) 333.
33. Riichiro Saito, Mitsutaka Fujita, G. Dresselhaus, and M. S. Dresselhaus, *Phys. Rev. B* **46**, 1804–1811 (1992).
34. G. S. Painter and D. E. Ellis, *Phys. Rev. B* **1**, 4747 (1970).
35. R. Saito, G. Dresselhaus, and M. S. Dresselhaus, *Physical Properties of Carbon Nanotubes* (Imperial College Press, London, 1998).
36. M. S. Dresselhaus, R. A. Jishi, G. Dresselhaus, D. Inomata, K. Nakao, and Riichiro Saito, *Molecular Materials* **4**, 27–40 (1994).
37. R. Saito, G. Dresselhaus, and M. S. Dresselhaus, *J. Appl. Phys.* **73**, 494 (1993).
38. K. Suenaga, C. Colliex, N. Demonty, A. Loiseau, H. Pascard, and F. Willaime, *Science* **278**, 653 (1997).
39. M. S. Dresselhaus, *Nature (London)* **391**, 19–20 (1998).
40. S. Wang and D. Zhou, *Chem. Phys. Lett.* **225**, 165 (1994).
41. C. H. Olk and J. P. Heremans, *J. Mater. Res.* **9**, 259–262 (1994).
42. T. Ebbesen. In *Fullerenes and Nanotubes*, edited by Pierre Delhaès and P. M. Ajayan (Gordon and Breach, Paris, 1998) Series: World of Carbon, Vol. 2.
43. S. J. Tans, M. H. Devoret, H. Dai, A. Thess, R. E. Smalley, L. J. Geerligs, and C. Dekker, *Nature (London)* **386**, 474 (1997).
44. M. S. Dresselhaus, G. Dresselhaus, P. C. Eklund, and R. Saito, *Physics World* **11**(1), 33–38 (1998).
45. L. Kouwenhoven, *Science* **275**, 1896 (1997).
46. S. J. Tans, R. M. Verschueren, and C. Dekker, *Nature* **393**, 49–52 (1998).
47. C. T. White and T. N. Todorov, *Nature (London)* **393**, 240 (1998).
48. S. Frank, P. Poncharal, Z. L. Wang, and W. A. de Heer, *Science* **280**, 1744 (1998).

49. L. Chico, V. H. Crespi, L. X. Benedict, S. G. Louie, and M. L. Cohen, Phys. Rev. Lett. **76**, 971–974 (1996).
50. W. Tian and S. Dalla, Phys. Rev. B **49**, 5097 (1994).
51. M. F. Lin and K. W.-K. Shung, Phys. Rev. B **51**, 7592 (1995).
52. M. Bockrath, D. H. Cobden, P. L. McEuen, N. G. Chopra, A. Zettl, A. Thess, and R. E. Smalley, Science **275**, 1922–1924 (1997).
53. S. J. Tans, M. H. Devoret, R. J. A. Groeneveld, and C. Dekker, Nature **394**, 761–764 (1998).
54. M. Bockrath, D. H. Cobden, J. Lu, A. G. Rinzler, R. E. Smalley, L. Balents, and P. L. McEuen, Nature (London) **397**, 598–601 (1999).
55. C. L. Kane and E. J. Mele, Phys. Rev. Lett. **78**, 1932 (1997).
56. H. Dai, E. W. Wong, and C. M. Lieber, Science **272**, 523–526 (1994).
57. T. W. Ebbesen, H. J. Lezec, H. Hiura, J. W. Bennett, H. F. Ghaemi, and T. Thio, Nature (London) **382**, 54–56 (1996).
58. L. Langer, V. Bayot, E. Grivei, J. P. Issi, J. P. Heremans, C. H. Olk, L. Stockman, C. Van Haesendonck, and Y. Bruynseraeede, Phys. Rev. Lett. **76**, 479–482 (1996).
59. M. S. Dresselhaus, Physics World **9**(5), 18–19 (1996).
60. R. Saito, G. Dresselhaus, and M. S. Dresselhaus, Phys. Rev. B **53**, 2044–2050 (1996).
61. Ph. Lambin, A. Fonseca, J. P. Vigneron, J. B. Nagy, and A. A. Lucas, Chem. Phys. Lett. **245**, 85–89 (1995).
62. J.-C. Charlier and Ph. Lambin, Phys. Rev. B **57**, R15037 (1998).
63. P. G. Collins, A. Zettl, H. Bando, A. Thess, and R. E. Smalley, Science **278**, 5335 (1997).
64. A. B. Kaiser, G. Dusberg, and S. Roth, Phys. Rev. B **57**, 1418 (1998).
65. J. Hone, M. S. Fuhrer, K. Khazeni, and A. Zettl, Phys. Rev. Lett. **80**, 5560 (1998).
66. L. Grigorian, K. A. Williams, S. Fang, G. U. Sumanasekera, A. L. Loper, E. C. Dickey, S. J. Pennycook, and P. C. Eklund, Phys. Rev. Lett. **80**, 5560 (1998).
67. R. S. Lee, H. J. Kim, J. E. Fischer, A. Thess, and R. E. Smalley, Nature (London) **388**, 255 (1997).
68. J. E. Fischer, H. Dai, A. Thess, N. M. Hanjani, D. L. Dehaas, and R. E. Smalley, Phys. Rev. B **55**, R4921 (1997).
69. P. Delaney, H. J. Choi, J. Ihm, S. G. Louie, and M. L. Cohen, Nature (London) **391**, 466 (1998).
70. Y. K. Kwon, S. Saito, and D. Tománek, Phys. Rev. B **58**, R133114 (1998).
71. L. Grigorian, G. U. Sumanasekera, A. L. Loper, S. Fang, J. L. Allen, and P. C. Eklund, Science (1999) submitted.
72. L. Grigorian, G. U. Sumanasekera, A. L. Loper, S. Fang, J. L. Allen, and P. C. Eklund, Phys. Rev. B **58**, R4195 (1998).
73. R. A. Jishi, L. Venkataraman, M. S. Dresselhaus, and G. Dresselhaus, Chem. Phys. Lett. **209**, 77–82 (1993).
74. E. Richter and K. R. Subbaswamy, Phys. Rev. Lett. **79**, 2738 (1997).
75. R. Saito, T. Takeya, T. Kimura, G. Dresselhaus, and M. S. Dresselhaus, Phys. Rev. B **57**, 4145–4153 (1998).
76. R. A. Jishi, D. Inomata, K. Nakao, M. S. Dresselhaus, and G. Dresselhaus, J. Phys. Soc. Jpn. **63**, 2252–2260 (1994).
77. M. S. Dresselhaus, G. Dresselhaus, M. A. Pimenta, and P. C. Eklund. pages 367–434, Blackwell Science Ltd., Oxford, UK, 1999. Analytical Applications of Raman Spectroscopy.
78. A. M. Rao, E. Richter, S. Bandow, B. Chase, P. C. Eklund, K. W. Williams, M. Menon, K. R. Subbaswamy, A. Thess, R. E. Smalley, G. Dresselhaus, and M. S. Dresselhaus, Science **275**, 187–191 (1997).
79. P. C. Eklund, J. M. Holden, and R. A. Jishi, Carbon **33**, 959 (1995).
80. E. Richter and P. C. Eklund, Phys. Rev. Lett. (1999) submitted.
81. Y. Saito, Y. Tani, N. Miyagawa, K. Mitsushima, A. Kasuya, and Y. Nishina, Chem.

- Phys. Lett. **294**, 593–598 (1998).
- 82. M. Sugano, A. Kasuya, K. Tohji, Y. Saito, and Y. Nishina, Chem. Phys. Lett. **292**, 575–579 (1998).
 - 83. H. Kuzmany, B. Burger, M. Hulman, J. Kurti, A. G. Rinzler, and R. E. Smalley, Europhys. Lett. **44**, 518–524 (1998).
 - 84. A. Kasuya, M. Sugano, Y. Sasaki, T. Maeda, Y. Saito, K. Tohji, H. Takahashi, Y. Sasaki, M. Fukushima, Y. Nishina, and C. Horie, Phys. Rev. B **57**, 4999 (1998).
 - 85. E. Anlaret, N. Bendjab, T. Guillard, C. Journet, G. Flamant, D. Laplaze, P. Bernier, and J-L Sauvajol, Carbon **36**, 1815–1820 (1998).
 - 86. H. Kuzmany, B. Burger, A. Thess, and R. E. Smalley, Carbon **36**, 709–712 (1998).
 - 87. H. Hiura, T. W. Ebbesen, K. Tanigaki, and H. Takahashi, Chem. Phys. Lett. **202**, 509 (1993).
 - 88. N. Chandrabhas, A. K. Sood, D. Sundararaman, S. Raju, V. S. Raghunathan, G. V. N. Rao, V. S. Satry, T. S. Radhakrishnan, Y. Hariharan, A. Bharathi, and C. S. Sundar, PRAMANA-Journal of Phys. **42**, 375–385 (1994).
 - 89. J. M. Holden, Ping Zhou, Xiang-Xin Bi, P. C. Eklund, Shunji Bandow, R. A. Jishi, K. Das Chowdhury, G. Dresselhaus, and M. S. Dresselhaus, Chem. Phys. Lett. **220**, 186–191 (1994).
 - 90. R. Saito, T. Takeya, T. Kimura, G. Dresselhaus, and M. S. Dresselhaus, Phys. Rev. B **59**, 2388–2392 (1999).
 - 91. Jean-Christophe Charlier. Private communication.
 - 92. M. A. Pimenta, A. Marucci, S. D. M. Brown, M. J. Matthews, A. M. Rao, P. C. Eklund, R. E. Smalley, G. Dresselhaus, and M. S. Dresselhaus, J. Mater. Research **13**, 2396–2404 (1998).
 - 93. M. A. Pimenta, A. Marucci, S. Empedocles, M. Bawendi, E. B. Hanlon, A. M. Rao, P. C. Eklund, R. E. Smalley, G. Dresselhaus, and M. S. Dresselhaus, Phys. Rev. B **58**, R16012–R16015 (1998).
 - 94. A. S. Barker and R. Loudon, Rev. Mod. Phys. **44**, 18 (1972).
 - 95. T. Pichler, M. Knupfer, M. S. Golden, J. Fink, A. Rinzler, and R. E. Smalley, Phys. Rev. Lett. **80**, 4729 (1998).
 - 96. A. M. Rao, P. C. Eklund, S. Bandow, A. Thess, and R. E. Smalley, Nature (London) **388**, 257 (1997).
 - 97. M. S. Dresselhaus and G. Dresselhaus, Advances in Phys. **30**, 139–326 (1981).
 - 98. J. L. Allen, G. Sumanasekara, A. M. Rao, A. Loper, and P. C. Eklund, J. Phys. Chem. (1999) submitted.
 - 99. G. Sumanasekara, J. L. Allen, A. M. Rao, S. Fang, and P. C. Eklund, J. Phys. Chem. (1999) submitted.
 - 100. M. S. Dresselhaus and G. Dresselhaus, Light Scattering in Solids III **51**, edited by M. Cardona and G. Güntherodt (Springer, Berlin, 1982) Vol. 51, Topics in Applied Physics.
 - 101. P. C. Eklund and G. L. Doll. In *Graphite Intercalation Compounds II: Transport and Electronic Properties*, edited by H. Zabel and S. A. Solin, (Springer, Berlin, 1992) Vol. 18, Springer Series in Materials Science, 105–162.
 - 102. M. S. Dresselhaus, G. Dresselhaus, K. Sugihara, I. L. Spain, and H. A. Goldberg, *Graphite Fibers and Filaments* (Springer, Berlin, 1988), Vol. 5, Springer Series in Materials Science.
 - 103. Z. Ya. Kosakovskaya, L. A. Chernozatonskii, and E. A. Fedorov, JETP Lett. (Pis'ma Zh. Eksp. Teor.) **56**, 26 (1992).
 - 104. M. R. Falvo, G. J. Clary, R. M. Taylor II, V. Chi, F. P. Brooks Jr, S Washburn, and R. Superfine, Nature (London) **385** (1997).
 - 105. M. Endo, K. Takeuchi, S. Igarashi, K. Kobori, M. Shiraishi, and H. W. Kroto, J. Phys. Chem. Solids **54**, 1841–1848 (1994).
 - 106. J. Tersoff and R. S. Ruoff, Phys. Rev. Lett. **73**, 676 (1994).
 - 107. R. S. Ruoff and D. C. Lorents, Carbon **33**, 925 (1995).
 - 108. J. W. Mintmire and C. T. White, Carbon **33**, 893 (1995).

109. B. I. Yakobson, C. J. Brabec, and J. Bernholc, Phys. Rev. Lett. **76**, 2511 (1996).
110. B. T. Kelly, in *Physics of Graphite*, (Applied Science, London, 1981).
111. D. H. Robertson, D. W. Brenner, and J. W. Mintmire, Phys. Rev. B **45**, 12592 (1992).
112. J. Tersoff, Phys. Rev. B **46**, 15546 (1992).
113. M. M. J. Treacy, T. W. Ebbesen, and J. M. Gibson, Nature (London) **381**, 678 (1996).
114. O. Lourie and H. D. Wagner, J. Mater. Res. **13**, 2418 (1998).
115. L. S. Schadler, S. C. Giannaris, and P. Ajayan, Appl. Phys. Lett. **73**, 3842–3844 (1998).
116. B. I. Yakobson and R. E. Smalley, American Scientist **85**, 324 (1997).
117. D. L. Carroll, P. Redlich, P. M. Ajayan, J. C. Charlier, X. Blase, A. De Vita, and R. Car, Phys. Rev. Lett. **78**, 2811–2814 (1997).
118. W. A. de Heer, A. Châtelain, and D. Ugarte, Science **270**, 1179 (1995); see also *ibid*, p. 1119.
119. A. G. Rinzler, J. H. Hafner, P. Nikolaev, L. Lou, S. G. Kim, D. Tománek, P. Nordlander, D. T. Colbert, and R. E. Smalley, Science **269**, 1550 (1995).
120. P. G. Collins and A. Zettl, Appl. Phys. Lett. **69**, 1969 (1996).
121. S. Fan, M. G. Chapline, N. R. Franklin, T. W. Tombler, A. M. Casswell, and H. Dai, Science **283**, 512–514 (1999).
122. J. Kong, H. T. Soh, A. M. Casswell, C. F. Quate, and H. Dai, Nature (London) **395**, 878–881 (1998).
123. A. C. Dillon, K. M. Jones T. A. Bekkedahl, C.-H. Kiang, D. S. Bethune, and M. J. Heben, Nature (London) **386**, 377 (1996).